Diabatic Divergence Profiles in Western Pacific Mesoscale Convective Systems

BRIAN E. MAPES

UCAR Visiting Scientist, NOAA Climate and Global Change Program, Program in Atmospheric and Oceanic Sciences, University of Colorado, Boulder, Colorado

ROBERT A. HOUZE JR.

Department of Atmospheric Sciences, University of Washington, Seattle, Washington

(Manuscript received 10 June 1994, in final form 8 December 1994)

ABSTRACT

Heating in the atmosphere can be expressed as diabatic divergence δ_d, which is nearly equal to the actual horizontal divergence δ in tropical convection. High-quality δ profile measurements from airborne Doppler radar "purls" in ten mesoscale convective systems (MCS) observed during TOGA-COARE are examined, and the mean profile is compared with rawinsonde array measurements. Young convective features have strong near-surface convergence, while older cells with better-developed downdrafts and stratiform precipitation areas have their peak convergence aloft. In the mean, then, surface flow is only weakly convergent or even divergent, so that the main convergence into MCSs is deep and peaked aloft, with a sharp "melting convergence" at 0°C. Divergence prevails above ~10 km altitude but was undersampled by the radar.

Unusual but well-sampled observations in the purl dataset include: a persistent, widespread δ profile feature in one well-sampled MCS (a cyclone rainband); oscillatory "reverberations" centered on the melting level, with ~3–4 km wavelength in the vertical; and a conspicuous absence of any high vertical wavenumber features other than the melting reverberations.

All three observations may be understood as consequences of the heating profile of convection adjusting itself to oppose environmental temperature perturbations. This adjustment is predicted by convective cloud conceptual models with diverse dynamical bases, and consequently is simulated by essentially all convective parameterization schemes. One foreseeable consequence of this mechanism is the downward development of initially elevated (cool core) depressions, a key stage in tropical cyclogenesis.

Simple linear models of Hadley and Walker circulations forced by observed MCS δ_d profiles illustrate the importance of the elevated convergence peak to large-scale circulations, particularly to low-level wind fields.

1. Introduction

Tropical deep convection constitutes the upward branch of vertical circulations on a wide range of spatial scales from mesoscale to planetary, and the vertical structure of convective heating largely defines the vertical structure of them all. The latent heat released in precipitating convection represents the harvest of solar energy from vast expanses of low-albedo tropical and subtropical ocean, but the vertical structure of this latent heating depends on internal processes within the relatively small areas undergoing deep convection.

Although heating is a fundamental quantity in thermodynamics, it is a secondary or derived quantity in observational meteorology. Localized heating in the tropical atmosphere is manifested not as a localized rising temperature, but as a sink of low potential temperature air in the lower troposphere and a source of high potential temperature air in the upper troposphere. The diagnosis of convective heating profiles is accomplished, in essence, by measuring the profile of δ—the divergence of the horizontal wind,[1] integrating vertically to get a mean vertical velocity, and multiplying by the nearly time-invariant static stability profile. Horizontal advection and local temperature changes are poorly measured but are minor contributors to diagnosed heating profiles (e.g., Frank and McBride 1989).

In this diagnostic process, important, well-measured high-wavenumber features of the divergence profile are deemphasized by the vertical integration: extrema in the profile of δ become merely inflection points in the resulting bland heating profiles. These high wavenumber features tend to get lost or distorted in diagnostic models of the tropical tropospheric circulation because studies of thermally forced flows generally use ideal-

Corresponding author address: Dr. Brian E. Mapes, University of Colorado, Campus Box 311, Boulder, CO 80309.
E-mail: mapes@monsoon.colorado.edu

[1] Throughout this paper the term "divergence" means horizontal divergence.

ized, rather than measured, heating profiles (e.g., Geisler and Stevens 1982; Kasahara 1984; Hartmann et al. 1984; DeMaria 1985; Schubert et al. 1991). When these idealized heating profiles are related to observations at all, it is typically only through reference to the altitude of the maximum heating.

Condensation minus evaporation is the dominant heating term in mesoscale convective systems (Houze 1982, 1989). However, the profile of this term is inseparably linked to the vertical mass flux profile in the convecting volume of the atmosphere. Theoretical and laboratory parcel and plume models explain only the grossest features of convective cloud-mass flux profiles. Ensemble models, from the simple updraft-only entraining plume ensemble of Yanai et al. (1973) to sophisticated process-laden cumulus ensemble models (e.g., Sui et al. 1994), do not predict mass flux profiles. Rather they adjust their numerous internal variables to match specified destabilization profiles. The moist, turbulent dynamics governing the profile of vertical mass flux (and therefore heating) are so inscrutably complex that we take a purely empirical approach to the question of tropical mesoscale convective system (MCS) heating profiles.

To proceed with this empirical inquiry, we first reformulate the concept of heating in terms of "diabatic divergence," δ_d. This approach, outlined in section 2, serves two purposes. First, δ_d is an interpretive device for divergence observations: scale analysis shows that the actual horizontal divergence measured in tropical convective regions is practically indistinguishable from δ_d. Second, the diabatic–adiabatic separation outlined herein is useful in approaching the unsolved problem of the interaction of convection with larger-scale motions. In a theoretical or model framework (section 6), it is possible to isolate and predict the small, diabatically forced, *adiabatic* vertical displacements which may stabilize and destabilize the atmosphere.

This paper presents δ profiles within ten mature MCSs, as measured by airborne Doppler radar during TOGA-COARE[2] using the technique described in section 3. Rawinsonde-derived δ profiles over the COARE Intensive Flux Array (IFA, base map in Fig. 1) confirm the major features and the representativeness of the airborne Doppler measurements (sections 4 and 5). The measured δ profiles are spectrally decomposed in terms of the vertical normal modes of the linearized primitive equations with realistic stratification. This spectral representation of δ is not merely an alternative way to look at the profile; plots of the spectral coefficients of a δ_d profile versus normal-mode gravity wave speed (e.g., Fig. 14a) have a clear, simple correspondence to the

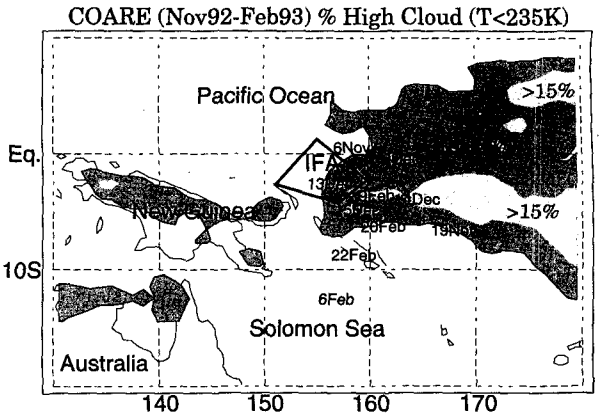

FIG. 1. Base map, 4-month mean percent high cloudiness (PHC), and approximate locations of the 10 flights from which Doppler radar purl data were analyzed. PHC, defined as the coverage of cloud tops colder than 235 K, is contoured at 10% and 15% to 15°S only.

temperature perturbations caused by a mesoscale heat source characterized by that δ_d profile (see Fig. 14b).

The analyses of sections 5c and 6 indicate that the overall mean MCS mass flux profile is closely related to the environmental stratification. MCS mass flux profiles are highly constrained by the requirement that they must satisfy mass continuity with the stratified atmosphere within which they are embedded. The δ_d profile adjusts to oppose environmental temperature anomalies, as discussed in section 6.

2. Diabatic and adiabatic vertical motions

a. Motivation and definitions

In this section, quantities relevant to vertical circulation (horizontal divergence, vertical velocity, and vertical displacement) are formally divided into diabatic and adiabatic parts following Raymond (1983), who in turn credits Ooyama (1971). A scale analysis is then invoked to show that the diabatic terms predominate in tropical convective regions, where temperature changes are much smaller than heating rates.

The thermodynamic equation in pressure coordinates is

$$C_p \frac{d_h T}{dt} - \omega\sigma = Q, \qquad (1)$$

where C_p is heat capacity at constant pressure, T is temperature, d_h/dt indicates local change plus horizontal advection, ω is pressure vertical velocity, σ is a static stability parameter, and Q is a bulk heating rate, which includes turbulent heat flux divergence as well as radiative and phase change heating. Rearranging Eq. (1), the total vertical velocity can be formally separated into diabatic and adiabatic parts:

[2] The Tropical Ocean–Global Atmosphere program's Coupled Ocean–Atmosphere Response Experiment (Webster and Lukas 1992).

$$\omega = \frac{-Q}{\sigma} + \frac{C_p d_h T/dt}{\sigma} \equiv \omega_d + \omega_a, \qquad (2)$$

where subscripts d and a indicate diabatic and adiabatic, respectively. The diabatic vertical motion ω_d is that vertical motion, which prevents T from changing in the presence of heating. Local and advective changes in T (and thereby in the static stability) are attributed *by definition* to the adiabatic vertical velocity ω_a. This definition makes the most sense for small-scale heating. As pointed out by one reviewer, a large-scale heating (e.g., global) would result in a rising temperature with $\omega = 0$. In that case ω_d and ω_a would both be large, but opposite in sign.

The diabatic and adiabatic divergence are related to their respective vertical velocities by the mass continuity equation:

$$\delta_{d,a} \equiv (\nabla \cdot \mathbf{V}_h)_{d,a} = -\frac{\partial \omega_{d,a}}{\partial p}, \qquad (3)$$

where $\mathbf{V}_h$ is the horizontal wind and p is pressure. It is also useful to define diabatic and adiabatic vertical displacements, relative to some initial state at time t_0, as the time integrals of the diabatic and adiabatic vertical velocities

$$\eta_{d,a} = \int_{t_0}^{t} \omega_{d,a} dt'. \qquad (4)$$

Here some scale analysis appropriate to tropical deep convection is necessary because δ_a is not necessarily smaller than δ_d on all space scales and timescales. Intense adiabatic divergence can occur in the tropical troposphere, leading to adiabatic vertical displacements and associated temperature changes. However, sounding data indicate that temperature perturbations rarely exceed 1°C in the free troposphere, while the latent heating associated with just 1 cm of rainfall corresponds to 2.5°C heating through the entire troposphere. The ratio of adiabatic to diabatic vertical displacements is thus

$$\epsilon \equiv \frac{\eta_a}{\eta_d} \sim \frac{\int \delta_a dtdp}{\int \delta_d dtdp} \sim \frac{CpT'}{\int Qdt} \approx \frac{T'}{2.5R}. \qquad (5)$$

Here T' is the temperature difference (in degrees Celsius) from the beginning to end of a time interval over which R centimeters of rain fall.

In a mesoscale convective system precipitating at the modest rate of 1 cm per hour, the upper limit on ϵ for the several-hour timescale that characterizes MCSs (and research flights) is less than 0.1. Therefore, $\eta_a \ll \eta_d$. Since η is the integral of δ over pressure and time [using (3) and (4)], $\delta_a \ll \delta_d$ *for deep, long-lasting heated circulations.* Adiabatic divergence is not necessarily small everywhere, but the fact that temperature perturbations (i.e., η_a) are small indicates that large values of δ_a cannot be deep and long lasting. Given the difficulty of measuring both deep temperature perturbations and divergence, it is fair to say that within measurement error $\delta \sim \delta_d$.

b. δ_d as thermal forcing in a primitive equation model

The linearized primitive equations can be reduced to a countable set of independent barotropic or "shallow water" equations—one for each of the vertical modes—by application of a normal-mode transform in the vertical (Fulton and Schubert 1985, hereafter FS85). This separation of horizontal and vertical structure is made possible by linearizing about a basic state with no motion. The vertical transform of FS85 finds numerical solutions for the normal modes of a hydrostatic atmosphere with a realistic temperature stratification, subject to the boundary conditions that geometric vertical velocity w equals 0 at 1000 mb and pressure vertical velocity ω equals 0 at some pressure level high in the atmosphere. We put the lid high enough (1 mb, the stratopause) that gravity wave reflections do not affect important features of the solutions presented herein.

In an atmosphere with constant buoyancy frequency N, vertical normal modes are sinusoidal in z, with corrections for the density variation with height (e.g., Geisler and Stevens 1982). In a realistic stratification, the modes are only quasi sinusoidal, with a local wavenumber or curvature that is large in regions of large N (such as the stratosphere and lower troposphere) and smaller in low-stability regions (such as the upper troposphere).

In the linearized primitive equations, each vertical mode behaves independently. The coefficients of the geopotential and wind fields for the nth mode (ϕ_n and $\mathbf{v}_n$) are governed by shallow water equations with "equivalent depth" H_n:

$$\frac{\partial \mathbf{v}_n}{\partial t} + f\mathbf{k} \times \mathbf{v}_n + \nabla \phi_n = \mathbf{0}$$

$$\frac{1}{gH_n}\frac{\partial \phi_n}{\partial t} + \nabla \cdot \mathbf{v}_n = \delta_{d_n}. \qquad (6)$$

Here f is the coriolis parameter, $\mathbf{k}$ is the vertical unit vector, and g is gravitational acceleration. The shallow water system (6) is nondispersive, with the wave speed given by $c_n = (gH_n)^{1/2}$. The ϕ_n and $\mathbf{v}_n$ governed by (6), which are functions of horizontal position and time only, can be multiplied by the nth mode's vertical structure function $\psi_n(p)$ and summed over n to obtain the full three-dimensional geopotential and wind fields. Temperature and vertical velocity fields can be constructed using the hydrostatic and mass continuity equations, respectively. In the FS85 transform, the

structure functions $\psi_n(p)$ and values of c_n are the eigenvectors and eigenvalues of a matrix whose size is a user-specified spectral truncation (here chosen to be 64). The results presented herein are insensitive to the spectral truncation provided it is large enough.

Note that *heating in the primitive equations appears in the transformed (6) as δ_{d_n}: the coefficients in the spectral expansion of the δ_d.* This presentation differs from that chosen by FS85, but follows from application of their (2.1), (2.4), (2.5), and (2.12) to their (2.14).

3. The airborne Doppler radar "purl" technique

a. Technical description

The divergence theorem applied to the horizontal plane states that divergence averaged over an area A is equal to the closed line integral of the perimeter-normal component of velocity V_n:

$$\frac{1}{A}\int \nabla\cdot\mathbf{V}\,dA = \frac{1}{A}\oint V_n\,dl. \qquad (7)$$

The divergence theorem is the basis for decades of research on cumulonimbus mass fluxes (e.g., Raymond et al. 1991 and references therein), and underlies almost all tropical heating profile diagnoses (e.g., Yanai et al. 1973; Frank and McBride 1989).

Doppler radar gives excellent estimates of one component of velocity in atmospheric volumes which contain sufficient precipitation-sized hydrometeors. For special sampling geometries, the component of wind measured by the Doppler radar can be precisely that required by the rhs of (7). Mapes and Houze (1993a, hereafter MH93a) used airborne Doppler radar data to obtain 93 profiles of divergence averaged over ~500-km^2 areas. In that study, the averaging areas were diamond-shaped regions nestled within the V-shaped intersections of a zigzagging flight pattern. The time required to sample one such area was nearly 20 minutes. Furthermore, radar data at fairly large ranges had to be used, so beam attenuation and beamwidth considerations limited the profiles to 1–2-km vertical resolution, often extending no higher than 10 km, with sea clutter adversely affecting the 0–1-km layer estimate.

In the present study, a circular geometry has been employed (Fig. 2). During TOGA-COARE flights in regions of widespread radar echo, the Doppler radar–bearing aircraft occasionally flew small circles, or purls,[3] along their otherwise generally straight flight tracks. During these purl maneuvers, each of which lasted about 4 minutes, the Doppler radar sampled the

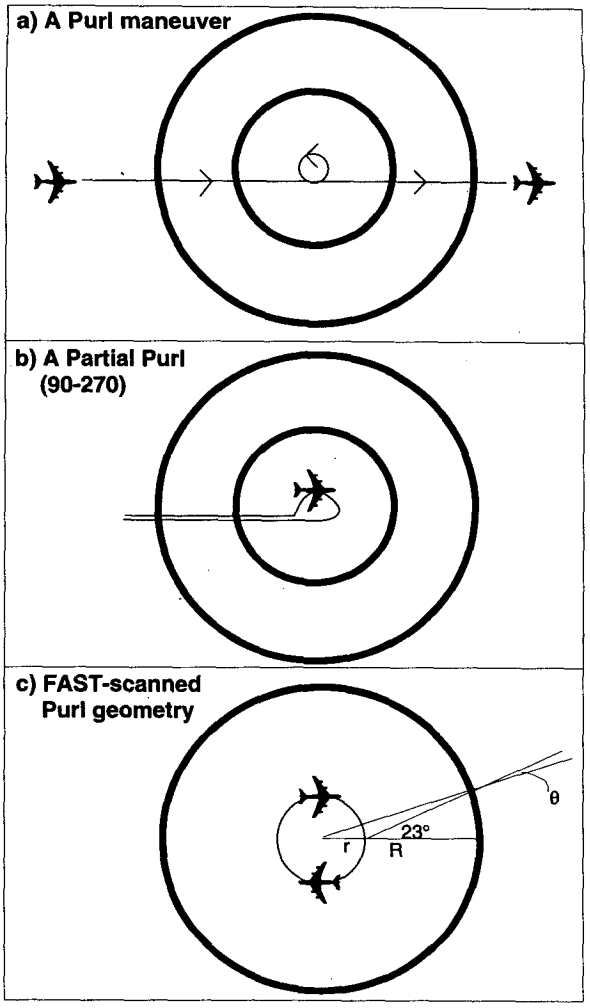

FIG. 2. Geometry of the airborne Doppler radar "purl" divergence measurement technique. Heavy circles indicate analysis cylinder boundaries, light lines indicate aircraft flight tracks.

component of hydrometeor velocity directed toward the aircraft. On the walls of an imaginary analysis cylinder centered on the purl, the Doppler radial velocities can be used to evaluate (7) as a function of height. The *horizontal* wind component in the rhs of (7) was estimated by removing the effects of an assumed hydrometeor fallspeed. To minimize the effects of error in this assumption, the analysis cylinders were chosen with large enough radius (>15 km) that the radar beams intersect it quasihorizontally even at altitudes far from the flight altitude. A trade-off exists between the vertical extent and resolution of the profiles, which favor small analysis cylinders, and the quasi-horizontal beam geometries and larger area averages obtained by using larger analysis cylinders.

There is one other consideration concerning the size of the analysis cylinders. In the Fore–Aft Scanning Technique (FAST) sometimes used during the purls,

[3] Definitions of *purl* in Webster's New Collegiate Dictionary include: (noun) a fine loop made in edging certain laces or lace braids; and (verb) to run swiftly round, to swirl, to move in circles. Hence, the word purl describes the aircraft's track in either space or time.

the Doppler radar alternately scanned conical sections ~23° fore and aft of the plane normal to the aircraft's axis or track. The geometry of a FAST-scanned purl is shown in Fig. 2c. The angle between the radar beam and the perimeter-normal direction is

$$\theta = \sin^{-1}\left(\frac{r}{R}\sin 23°\right) \approx \frac{r}{R}\cdot 23°, \qquad (8)$$

where r is the purl radius and R is the analysis cylinder radius. The wind components normal and tangential to the perimeter of the analysis cylinder, V_n and $V_{\tan}$, are related to the Doppler radial velocity V_r by

$$V_n \cos\theta = V_r - V_{\tan} \sin\theta. \qquad (9)$$

Because θ alternates between positive and negative, the $V_{\tan}$ contributions by fore and aft beams cancel each other when V_n from (9) is substituted into (7). In the final analysis, then, FAST scanning requires merely that one divide the line integral of V_r by the constant, near-unity factor $\cos\theta$.

Finally, it should be noted that with the radar scanning both to the right and left of the track, an aircraft needs only to traverse a semicircle, that is, at least 180° of aircraft heading angle, in order to render possible a purl computation. Hence the "90–270" turnaround maneuvers (Fig. 2b) frequently executed in the TOGA-COARE aircraft flights can also yield divergence profiles as long as radar scatterers were plentiful enough along the walls of some analysis cylinder. Of course, the less time spent in the turn, the sparser the data density, and hence the noisier the divergence estimate. In what follows, no distinction between full, partial, and FAST-scanned purls is made. No systematic differences among these three types of measurements are evident.

The line integral (7) was evaluated as a discrete sum within layers 500 m in depth, each Doppler datum being assigned a height based on idealized beam geometry. Automated Doppler velocity dealiasing was used. The results were excluded if the largest angular data gap on the analysis circle exceeded 60° (equal to the angular data gap in hexagonal rawinsonde arrays often used to measure divergence). As in MH93a, three independent calculations were made using the three radar range gates centered on the actual range of the analysis cylinder. Differences among the three give an indication of the uncertainty in the measurement due to Doppler radar uncertainty. The three estimates have been carried through all calculations, and all three estimates are plotted together in the divergence profile plots.

b. *Sampling considerations*

The greatest problem with airborne Doppler radar datasets, far more important than the small geometrical corrections described in the previous section, is the interpretation of the sample. The sampling issue can be divided into two separate questions: the representativeness of the particular MCSs that were sampled and the space–time sampling within the systems.

1) REPRESENTATIVENESS OF THE PURL-SAMPLED MCSs

By the nature of the method, purls were only performed in aircraft-accessible mesoscale systems with substantial stratiform rain areas. The COARE aircraft program was organized to sample the entire size spectrum of satellite-observed "cloud clusters," defined as contiguous areas of satellite-observed cloud-top temperature $T_{ct} < 208$ K (TCIPO 1992; Mapes and Houze 1992, 1993b). Clouds with $T_{ct} < 208$ K were invariably associated with precipitation.[4] However, frequent small showers without 208 K cloud tops, observed in the COARE region by shipborne radars, may have contributed ~10% of COARE rainfall. The purl divergence profiles represent only the δ_d contributed by cloud systems with $T_{ct} < 208$ K, and furthermore are highly biased toward the larger-sized cloud clusters. All ten flights analyzed herein fell within the three largest cloud-cluster-size quartiles of the 208 K cloud area. In short, *the purl-sampled MCSs do not represent all COARE convection, only that occurring in the larger, deeper mesoscale systems.*

We note, however, that the mean δ_d profile within these larger MCSs is of special relevance as a *perturbation* heating, that is, the heating *difference* between the active and inactive parts of two important oscillations: diurnal and intraseasonal. Mapes and Houze (1993b) showed that intraseasonal variability of the frequency of occurrence of large cloud clusters is considerably greater than that of smaller ones. They also found that the diurnally modulated occurrence of large MCSs accounts for the vast majority of the diurnal cycle in high cloudiness over the open ocean in the COARE region. In a study of middle atmosphere diurnal tides, Williams (1994) found that a two-mode (convective + stratiform) heating profile characteristic of MCSs, oscillating diurnally, excites more realistic tides in a model than does a one-mode heating profile that may be more typical of the total convective heating field.

2) SPACE–TIME SAMPLING WITHIN THE SAMPLED MCSs

The growing and mature stages of the life cycles of large MCSs occur primarily in the hours before dawn, corresponding to the hours of most frequent heavy rainfall events (e.g., Janowiak et al. 1994). For this reason, the COARE flights studied herein all occurred during

[4] Of course, the association was not always instantaneous, pixel by pixel, or proportional to rainfall intensity.

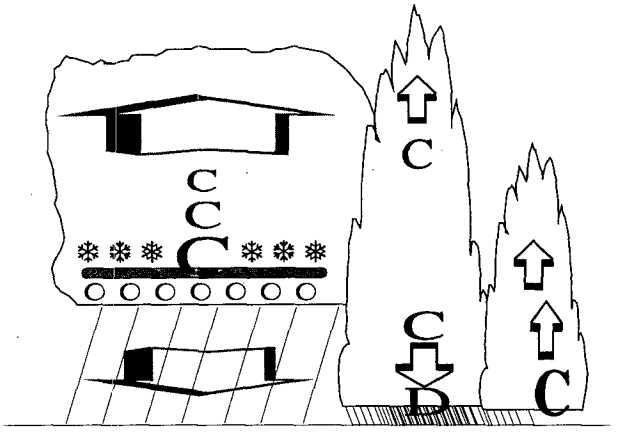

FIG. 3. Schematic summary of the convergence features observed in this study and in MH93a. Intense surface convergence prevails in young convective cells, while elevated convergence and surface divergence characterize older cells with their well-developed convective downdrafts. Midlevel convergence, with its peak value atop the melting layer, is observed in stratiform rain areas. Arrows indicate vertical winds associated with the convergence–divergence features.

approximately 0000 to 1000 LST. The MCSs were already well organized by the time the aircraft reached them and often weakened toward the ends of the flights. As a result, temporal sampling in these MCSs is biased toward the mature and decaying stages (Leary and Houze 1979) of the MCS life cycle. Fortunately, the mature and late stages of the life cycle contribute most of the total heating by MCSs (Frank and McBride 1989).

Furthermore, mature MCSs contain all types of precipitation processes, including vigorous young convective areas, "intermediary" areas composed of older convective cells, and stratiform rain areas. Convective lines or patches within an MCS typically evolve, via intermediary structures, into stratiform precipitation areas. The life cycle of an MCS is, in a sense, the aggregate of the life cycles of its embedded individual mesoscale precipitation features (MPFs, Leary and Houze 1979). An MCS is primarily composed of convective features early on in its life until a mature state develops, with new convective lines or areas regenerating at the same rate that the old ones evolve into stratiform precipitation. After the regeneration of new convective areas slows, the MCS "decays," becoming increasingly composed of stratiform precipitation which eventually rains out and dissipates.

MH93a found that in each of these three categories of local precipitation type (convective, intermediary, and stratiform), very similar divergence profiles prevailed, within a broad range of MCS types, in various synoptic settings within the Australian monsoon (see also section 4a). Apparently, a quasi-universal convective to stratiform precipitation development process underlies the diverse variety of mesoscale convective system morphologies observed in the atmosphere (e.g., Houze et al. 1990). Hence, a sample biased toward the mature stages of the MCS life cycle may still contain a complete sample of all stages of the deep convective process.

TOGA COARE flight plans were designed to sample all the component parts of MCSs (TCIPO 1992). On each flight, purls were first performed by a single aircraft during an initial survey of the target MCS, after which time multiple aircraft were brought together for an intensive convective sampling period. Numerous partial purls (Fig. 2b) and some full purls were performed during the multiaircraft "convective" and subsequent "whole system" or "whole MCS life cycle" sampling periods. After the multiaircraft sampling, the last Doppler-equipped aircraft made a final survey, performing more purls before returning to base. Of course, many decisions on purl placement were made subjectively by the scientists aboard the aircraft based on real-time radar reflectivity maps. *But their guiding principle was to try to sample the whole range of precipitation structures occurring in the MCSs of the COARE region.*

4. Airborne Doppler purl results

a. Convective, intermediary, and stratiform profiles

Figure 3 shows a schematic summary of the major convergence levels in the various types of precipitating cloud, which together make up an MCS, as gleaned from the divergence measurements of MH93a and the present study (see also Houze 1993, Fig. 9.62). Near-surface convergence characterizes young growing cumulonimbus towers, while elevated convergence predominates in older, heavily precipitating cells with well-developed downdrafts. An upper-tropospheric convergence is sometimes seen at the base of elevated ascending motions near 10-km altitude. Finally, midlevel convergence prevails in stratiform precipitation, with the most intense convergence just above the melting level, where sustained intense cooling takes place (see section 4c.2 below).

b. Flight by flight mean profiles

The purls from ten TOGA-COARE aircraft missions have been analyzed, comprising a total of 143 purls from the two U.S. NOAA WP-3D aircraft. Most of the missions contained about ten purls, while the flight of 9 February had the greatest number, 35. Each individual purl profile has considerable structure, a snapshot of the complex instantaneous field of updrafts and downdrafts within the cylinder. In this paper we present only space and time mean profiles (except for the examples in Figs. 7 and 9) because of their relevance to larger-scale atmospheric circulations.

The mean purl-derived δ profiles for each of the COARE flights are shown in Figs. 4 and 5 for the smallest and largest practicable analysis cylinder sizes (30- and 60-km diameters), respectively. Although the

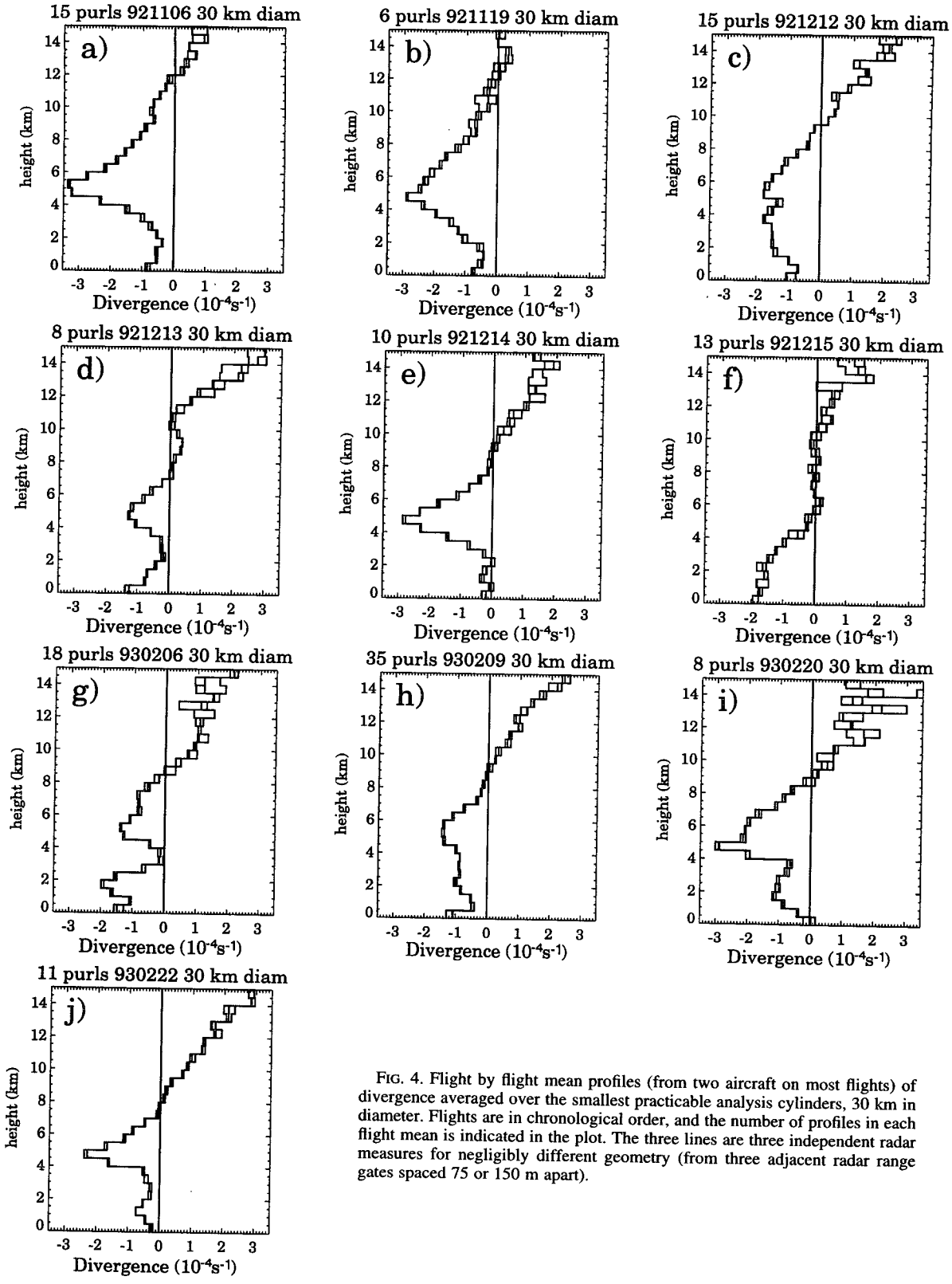

FIG. 4. Flight by flight mean profiles (from two aircraft on most flights) of divergence averaged over the smallest practicable analysis cylinders, 30 km in diameter. Flights are in chronological order, and the number of profiles in each flight mean is indicated in the plot. The three lines are three independent radar measures for negligibly different geometry (from three adjacent radar range gates spaced 75 or 150 m apart).

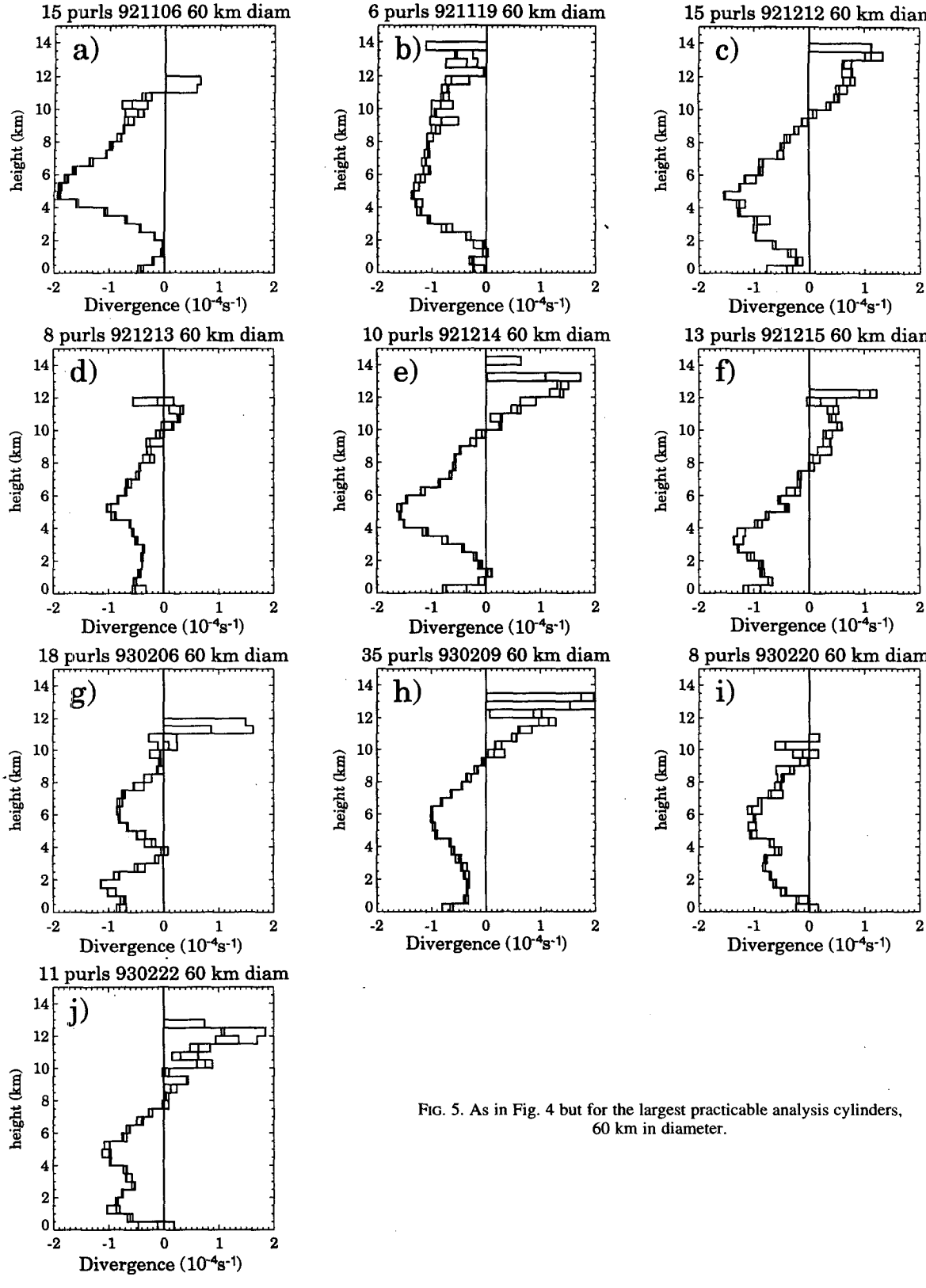

FIG. 5. As in Fig. 4 but for the largest practicable analysis cylinders, 60 km in diameter.

larger cylinders sampled four times the area of the smaller ones, the resulting mean profiles are quite similar, though somewhat weaker in amplitude and smoother as a result of the widening of the beam with range (cf. Figs. 4, 5). This near scale-independence indicates that the *averaged* results are not too sensitive to the particular locations of the purls.

All the flight-mean profiles consist of a deep layer of convergence, generally up to 8–10-km altitude, with the peak convergence usually just above the melting level (~4.7 km). This "melting convergence" peak is very sharp in some cases, especially on its lower edge (discussed in section 4c.2 below). The midlevel convergence peak is primarily contributed by stratiform precipitation areas, as seen in MH93a and many other studies (reviewed by Houze 1989). A secondary convergence peak below 4 km is present in many of the profiles, particularly for flights such as 15 December and 22 February, on which a great deal of vigorous, young convection was sampled. This low-level, but elevated, convergence is also familiar from the convective precipitation area profiles in MH93a. The convergence near 10 km seen in the "intermediary" precipitation area profiles of MH93a appears in some of the flight-mean profiles of Figs. 4–5 as a convergent kink in the profile (Figs. 4e, f) if not an actual convergence peak (as in Figs. 4a,d). Surface clutter renders Doppler radar measurements uncertain at very low levels, so the boundary-layer values (0–500 m layer) are not to be trusted.

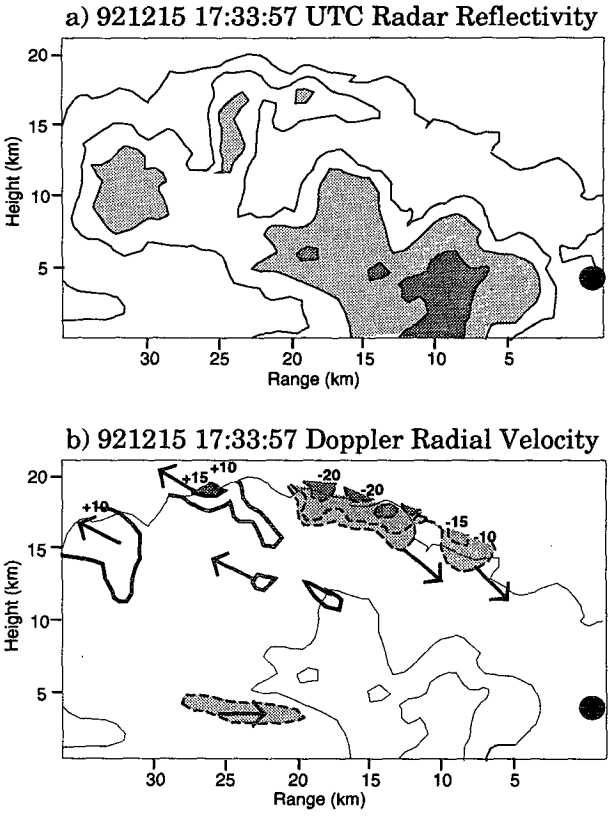

FIG. 6. A radar cross section showing intense divergence atop an extremely tall echo on 15 December. Heavy dot indicates radar location. (a) Radar reflectivity, 10 dbZ contours. Light shading indicates values >30; dark shading, values >40. (b) Doppler radial velocity, contoured at ±10, 15, and 20 m s^{-1}. Light shading indicates values <−10; dark shading, < −20 or >15. Arrows indicate the radial direction at several points.

c. *Notable features of the profiles*

1) THE MISSING UPPER-TROPOSPHERIC DIVERGENCE

Divergence turns positive somewhere near 8–10 km in most of these profiles then continues to increase with height. Nonetheless, the profiles are dominated by convergence, especially if one considers the density decrease with height (see Fig. 11, plotted against pressure). This mass-convergence imbalance in the measurements arises from the fact that *divergence aloft is inevitably undersampled by Doppler radar,* even in cases with very deep echoes.

Consider Fig. 6, a cross section through a particularly deep and intense patch of convection on 15 December (with definite stratosphere–troposphere exchange ramifications). The Doppler velocity field has its peak values right along the top of the radar echo near 20-km altitude. In this case, the 35 m s^{-1} radial velocity difference across 10 km indicates a divergence of 35×10^{-4} s^{-1} contributed by one component of the flow alone, a value that would be off the scale of the plots in Fig. 4 by a factor of 10. Such intense echo-top divergent flows were frequently observed in individual sweeps of the radar. Such observations indicate that strong divergence probably extended well into the air above echo top, rendering the use of echo-top boundary conditions in kinematic determinations of vertical velocity very dubious. Large vertical velocities at echo top are also evident in vertical incidence Doppler radar data from Australian monsoon MCSs (not shown) and in wind profiler data from convection over coastal north Australia (Cifelli and Rutledge 1994).

2) INTENSE SHALLOW CONVERGENCE ATOP THE MELTING LEVEL

Many stratiform-region purls in COARE were characterized by very intense shallow layers of convergence at the 0°C level, near 4.5–5-km altitude (even in flight means: Figs. 4a,e,i). Profiles of divergence from three individual purls, on different days, are shown in Fig. 7 along with contoured frequency by altitude diagrams (CFADs, Yuter and Houze 1994) that summarize the radar reflectivity contents of the analysis cylinders. All three echo volumes are characterized by narrow frequency distributions of radar reflectivity at all heights, with a strong radar brightband near the melting level characteristic of stratiform precipitation. In all three

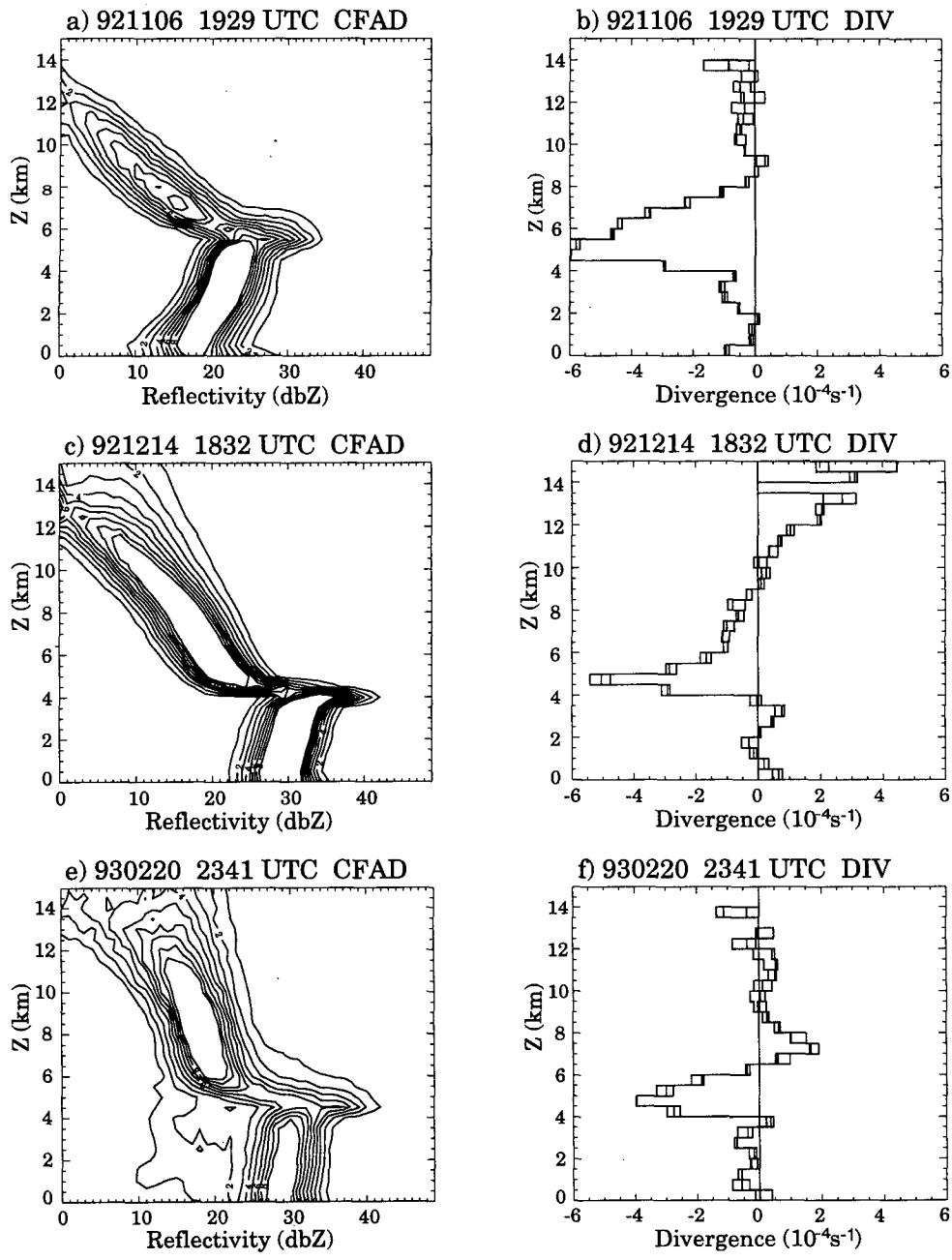

FIG. 7. Three purls (30-km diameter) illustrating "melting convergence." Left column (a), (c), (e): contoured frequency by altitude diagrams (CFADs, Yuter and Houze 1995) summarizing the radar reflectivity contents of the three cylindrical volumes. The contoured field is the fraction of the cylinder's area with the indicated dbZ value at each altitude (units: percent of the area of the cylinder per dbZ). Right column (b), (d), (f): cylinder area-averaged divergence profiles.

cases, strong convergence is seen in the 4.5–5-km layer, with a steep gradient on the lower side of the peak. Midlevel convergence in stratiform precipitation is ubiquitous (e.g., Houze 1989) and is thought to be associated with mean mesoscale ascent in the upper troposphere and mean mesoscale descent in the lower troposphere.

Equations (2) and (3) state that there is a large negative diabatic divergence at the 0°C level (near 4.7 km) because of the large value of $\partial(Q/\sigma)/\partial p$ there. The observations of intense convergence presented in Fig. 7 constitute a qualitative confirmation of the $\delta \sim \delta_d$ interpretation of divergence measurements, even in the case of this shallow layer.

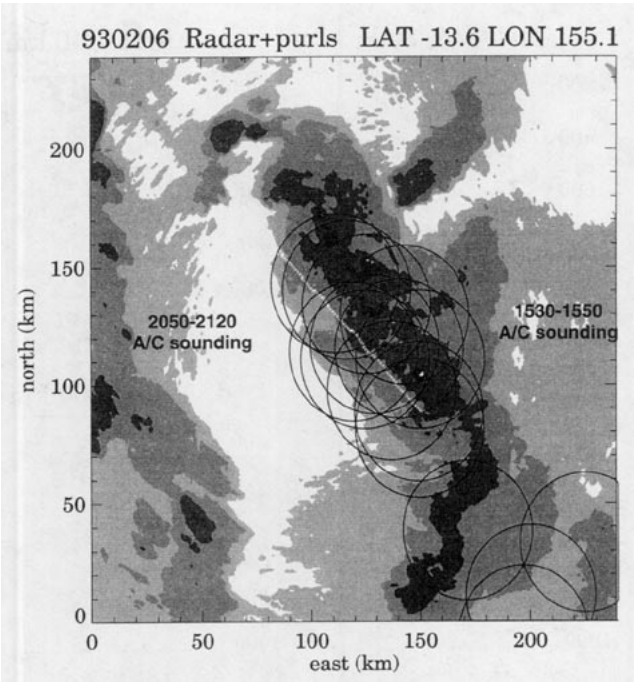

FIG. 8. Time-composite radar reflectivity map from 1741–1756 UTC 6 February 1993. Shaded contours are 10, 20, 30, and 40 dbZ. The white line is the flight track from the period of the time composite. Black circles indicate all purl analysis cylinders of 50-km diameter, spanning a ~6-h sampling period centered on the time of the image. Purl circles have been translated to their rainband-relative positions at the time of the image using a storm motion of 15 km h^{-1} eastward. The lower left corner is at 13.58°S, 155.09°E.

Wavelike oscillations of δ in the vertical, with a wavelength of approximately 4 km, can also be detected in the profiles in Fig. 7. These examples are by no means conclusive, but because of its persistence this vertical "reverberation" of the melting signal comes through clearly in averaged profiles. Possible reasons for its existence are discussed in section 6b.

3) THE UNUSUAL PROFILES OF 6 FEBRUARY

The most unusual MCS-mean profiles are those from the 18 purls obtained on 6 February (Figs. 4g and 5g). The 6 February case was also a geographical outlier (Fig. 1). On that date, a four-aircraft flight was conducted in a cyclone rainband near 12°S in the Solomon Sea, 400–500 km northeast of tropical cyclone Oliver. Unusually strong near-surface convergence was present, along with near-zero or even positive values of divergence at 3–4 km (Figs. 4g and 5g). Although somewhat similar features appear in Figs. 4d and 4i, those profiles represent only eight purls each and differ substantially from their corresponding larger area averages of Figs. 5d and 5i.

The case of 6 February is summarized in Fig. 8, a radar reflectivity image from a midflight time period, with all the analysis cylinders of 50-km diameter superposed. The data span a 6-h period, during which time the rainband moved slowly eastward at 15 km h^{-1}. The purl coverage is quite dense in the rainband.

The convergence–divergence anomaly couplet at low levels was a persistent feature throughout the rainband's spatial and temporal extent. Two contrasting purls from 6 February are shown in Fig. 9: a predominantly convective purl, characterized by a wide distribution of reflectivity at all heights (Fig. 9a), for which the near-surface convergence (Fig. 9b) is not necessarily surprising, and a predominantly stratiform purl, with its narrow reflectivity distribution (Fig. 9c), for which the low-level convergence–divergence couplet (Fig. 9d) is more out of character.

At first we suspected that this represented long-sought evidence of "large-scale forcing," that is, an underlying, larger-scale upward velocity that happened to be detectable within the rainband simply because the air there contained radar scatterers. But scale analysis indicates that it must be viewed as a diabatic divergence: even the small values on Fig. 9d indicate a vertical velocity of ~0.1 m s^{-1} at 2-km altitude, which, if occurring in the clear air just outside the rainband, would cause the temperature to drop several degrees over the duration of the flight. *This feature can only be explained as a perturbation of the mass flux and therefore the heating profile in the rainband convection, not as an underlying larger-scale vertical motion.*

Previous studies of convective clouds have attributed divergence (detrainment) anomalies to anomalies in

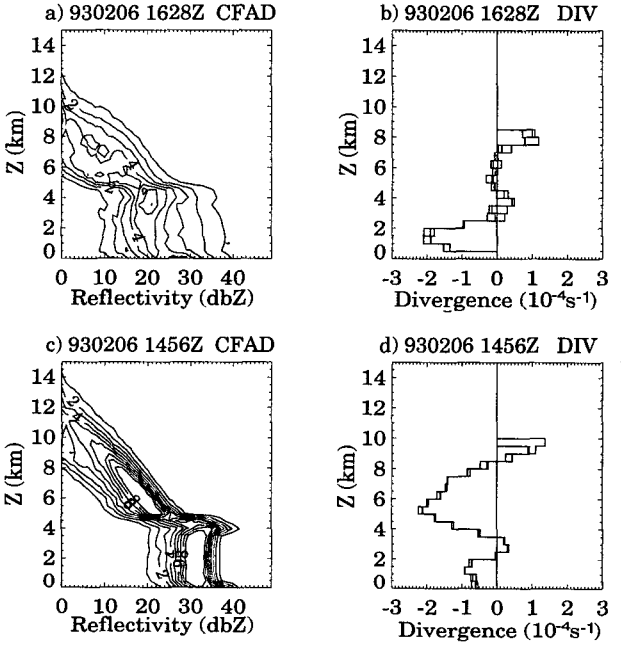

FIG. 9. Two purls from 6 February, one convective (panels a and b) and one predominantly stratiform (c), (d). As in Fig. 7.

the environmental stratification profile (Bretherton and Smolarkiewicz 1989; Taylor and Baker 1991; Raymond and Blyth 1992), a theory that seems to explain the present result as well. Aircraft temperature soundings (Fig. 10) show that the air below about 3 km was anomalously cool, while the temperature above 3 km was anomalously warm compared to the environment of the very heavily purl-sampled MCS of 9 February. Since the mean of the 35 purls of 9 February (Figs. 4h, 5h) is very much like the mean of all 146 COARE purls (Fig. 11), the comparison of 6 and 9 February is a particularly appropriate one. That the low-level cool anomaly on 6 February was persistent and widespread is also evident in the more plentiful, but less reliable, dropwindsonde data (not shown).

The mesoscale convection of 6 February was thus a well-sampled example of the interaction of convective mass flux (and hence heating) profiles with the ambient temperature field. This important relationship is the subject of section 6.

5. Grand mean divergence profiles

a. Grand mean purl profiles

Figure 11 displays, for the four different analysis cylinder sizes, the mean of all 143 purl divergence profiles. The profiles are plotted against pressure rather than height to indicate the mass divergence contribution by each 500-m measurement layer. All four profiles are very similar, indicating that the mean results are not very sensitive to the particular locations of the purls within the sampled MCSs. The major differences among the profiles are simply that the larger-cylinder analyses are smoother, owing to vertical beamwidth considerations. For this reason, the small-cylinder mean profile (Fig. 11a) is our best estimate of mean divergence in the mature MCSs sampled.

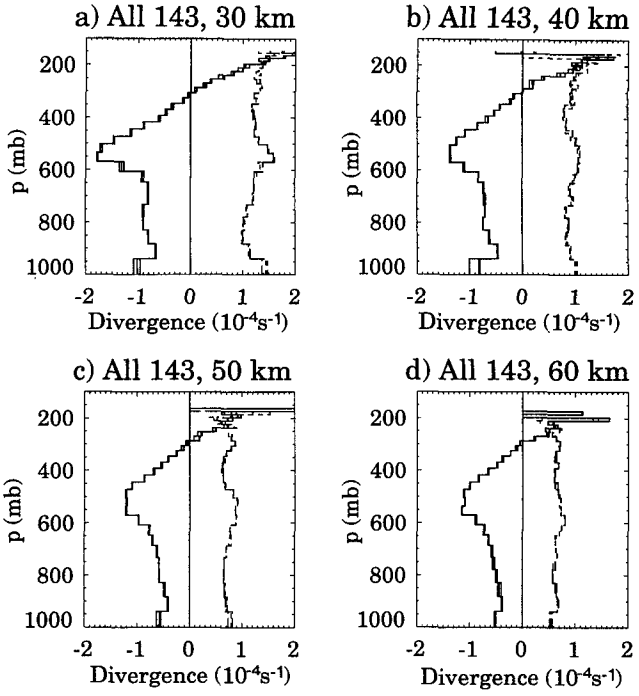

FIG. 11. The mean divergence profiles (solid lines) and standard deviations (dashed, positive) for all 143 purls analyzed in this study. The four panels are from analysis cylinders of diameters 30, 40, 50, and 60 km.

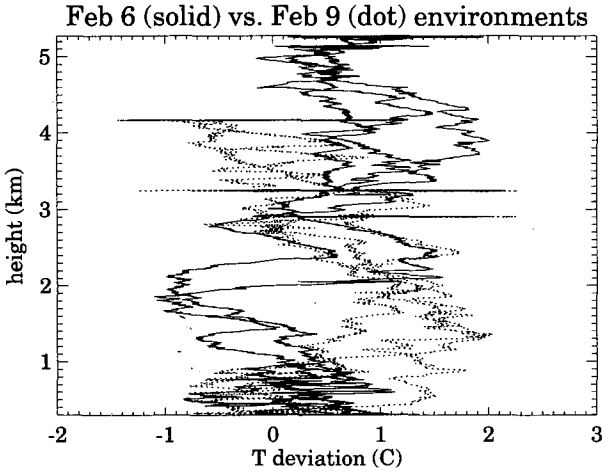

FIG. 10. Aircraft-measured temperature profiles on 6 and 9 February (solid and dotted lines, respectively), expressed as deviations from the reference profile $T_{ref} = 26 - \Gamma z$, where z is height and Γ is 5.435°C km^{-1}. The 6 February data are 1500–1600 and 2000–2200 UTC from U.S. NOAA P3 #N43RF and 1534–1551 UTC from the NCAR Electra (above 3300 m, highest temperatures). The 9 February data are 2100–2156 UTC from N43RF and 1948–2038 UTC from the NCAR Electra. Horizontal lines are from horizontal flight segments on 9 February.

A deep layer of convergence prevails throughout the lower and middle troposphere, with its peak near 550 mb (the melting level). A secondary lower-tropospheric convergence peak is apparent at 800 mb in the smaller-cylinder analyses. The level of nondivergence is at ~300 mb, with divergence observed above that. Data amount and quality deteriorate rapidly above the 200-mb level, especially for the larger cylinder sizes. These results are broadly consistent with the findings of MH93a. The surface convergence value must be viewed with caution, as sea clutter affected some of the Doppler data in the lowest 500 m. Nonetheless, it is clear that convergence into these TOGA-COARE mesoscale convective systems was very deep, with the mean surface convergence playing only a small part, a result known at least since the time of Ruprecht and Gray (1976).

The standard deviation of divergence (dashed lines in Fig. 11) has three maxima within the well-measured levels of the troposphere: one near the surface (though

the lowest level must be considered suspect, owing to radar surface clutter); another near 550 mb associated with the intermittent "melting convergence" at that level (e.g., Fig. 7); and one near 300 mb (clearest in Fig. 11c) associated with the intermittent convergence near 10-km altitude, characteristic of "intermediary" precipitation areas (MH93a). Note that the standard deviation is indicative of *meteorological variability* among the 143 purls, not of uncertainty in the divergence measurements. Measurement uncertainty is better indicated by the generally very small spread of the three independent Doppler estimates (the three solid and three dashed lines in Fig. 11) and by level to level differences since the levels are independently measured.

Examination of the flight tracks and horizontal radar echo maps suggests that the purl sampling succeeded in capturing all the component parts of the MCSs investigated by the aircraft, although stratiform precipitation may have been oversampled relative to convective precipitation. Ultimately, it is necessary to look to other, larger-scale data sources to see if the purl profiles are really representative of the whole systems or of COARE deep convective δ profiles generally.

b. *Larger-scale estimates of δ_d profiles*

Rawinsonde-derived wind divergence provides the most direct way to estimate δ_d on larger scales. Because of the great distances separating rawinsonde point measurements, inaccuracy in evaluating expressions like (7) is inevitable, so mass-balance corrections plus time averaging must be employed to obtain the best possible estimates. Objective analyses of divergence every 6 hours, averaged over the COARE Intensive Flux Array (IFA, see Fig. 1), were obtained courtesy of Xin Lin and Prof. R. Johnson of Colorado State University. The analyses were created by gridding the omegasonde-measured winds at 25-mb pressure intervals, computing divergence (adjusted so that vertical velocity is zero at 75 and 1000 mb), and averaging the values at all gridpoints within the IFA. Since soundings were launched around the perimeter of the IFA, these area-mean divergence profiles should be reasonably well measured.

We have examined all 480 of these divergence profiles, along with corresponding hourly infrared satellite images. Sixteen cases were selected in which the IFA contained cloud clusters with substantial areas of very cold ($T_{ct} < 208$ K) cloud top. These cases are listed in Table 1, and illustrated in Fig. 12. A wide variety of cloud cluster morphologies is represented.

The composite divergence profile from the 16 MCS-affected periods listed in Table 1 is shown in Fig. 13 (solid line). The lower-tropospheric convergence peaks at 675 mb, somewhat lower than the purl convergence peak (Fig. 11), while divergence prevails from 350–100 mb and in a thin layer at the surface. To assure that the composite process captured the entire MCS life cycle, we also plotted an "extended life cycle" composite, consisting of the MCS composite plus all analysis times immediately before and after the times listed in Table 1 (long-dashed line in Fig. 13). That profile is quite similar in shape but weaker in amplitude, indicating that the compositing process did not miss any strong signals early or late in the life cycles. The short-dashed curve on Fig. 13 is the leading empirical orthogonal function (EOF) of the entire dataset of 480 divergence profiles (the amplitude is arbitrary). It bears a remarkable resemblance to the MCS composite profiles, suggesting that the leading source of variance in the IFA divergence profiles is simply the intermittency of strong convective activity like that included in this composite.

The stronger midlevel convergence peak in the radar profiles relative to the rawinsonde profiles suggests that the purl sampling did overemphasize stratiform precipitation with its midlevel (~550 mb) convergence. The absence of a strong melting convergence in the IFA profiles is not surprising given the scale of the measurement and the slow propagation speed of the melting-associated divergence signal (Fig. 14).

TABLE 1. The begin and end times (at 6-h resolution) of 16 time intervals during which the Intensive Flux Array (IFA, map in Fig. 1) contained mesoscale convective systems. Divergence profiles for all analysis times within these intervals were averaged to obtain the MCS composite profile of Fig. 13.

0000 UTC 11 November	0600 UTC 12 November
1800 UTC 23 November	0600 UTC 24 November
1200 UTC 11 December	0000 UTC 12 November
1200 UTC 15 December	0600 UTC 16 December
0000 UTC 17 December	0600 UTC 17 December
1200 UTC 20 December	0600 UTC 21 December
1200 UTC 22 December	0000 UTC 23 December
0600 UTC 24 December	0600 UTC 25 December
1200 UTC 26 December	0600 UTC 27 December
0600 UTC 29 December	1200 UTC 29 December
1800 UTC 3 January	0000 UTC 4 January
0000 UTC 19 January	0000 UTC 20 January
0000 UTC 11 February	0000 UTC 12 February
1200 UTC 19 February	0000 UTC 20 February
1200 UTC 24 February	0000 UTC 25 February
0600 UTC 25 February	0000 UTC 26 February

c. *Circulations forced by the observed δ_d profiles*

1) VERTICAL MODE SPECTRA OF δ_d PROFILES AND THE SWITCHED-ON HEATING SOLUTION

As discussed in section 2, the measured divergence profiles can be interpreted as diabatic divergence δ_d, which appears as a thermal forcing in the transformed linear primitive equations. Spectral transforms of the Doppler radar purl and IFA-MCS composite sounding profiles of δ (from Figs. 11a and 13) are plotted in the

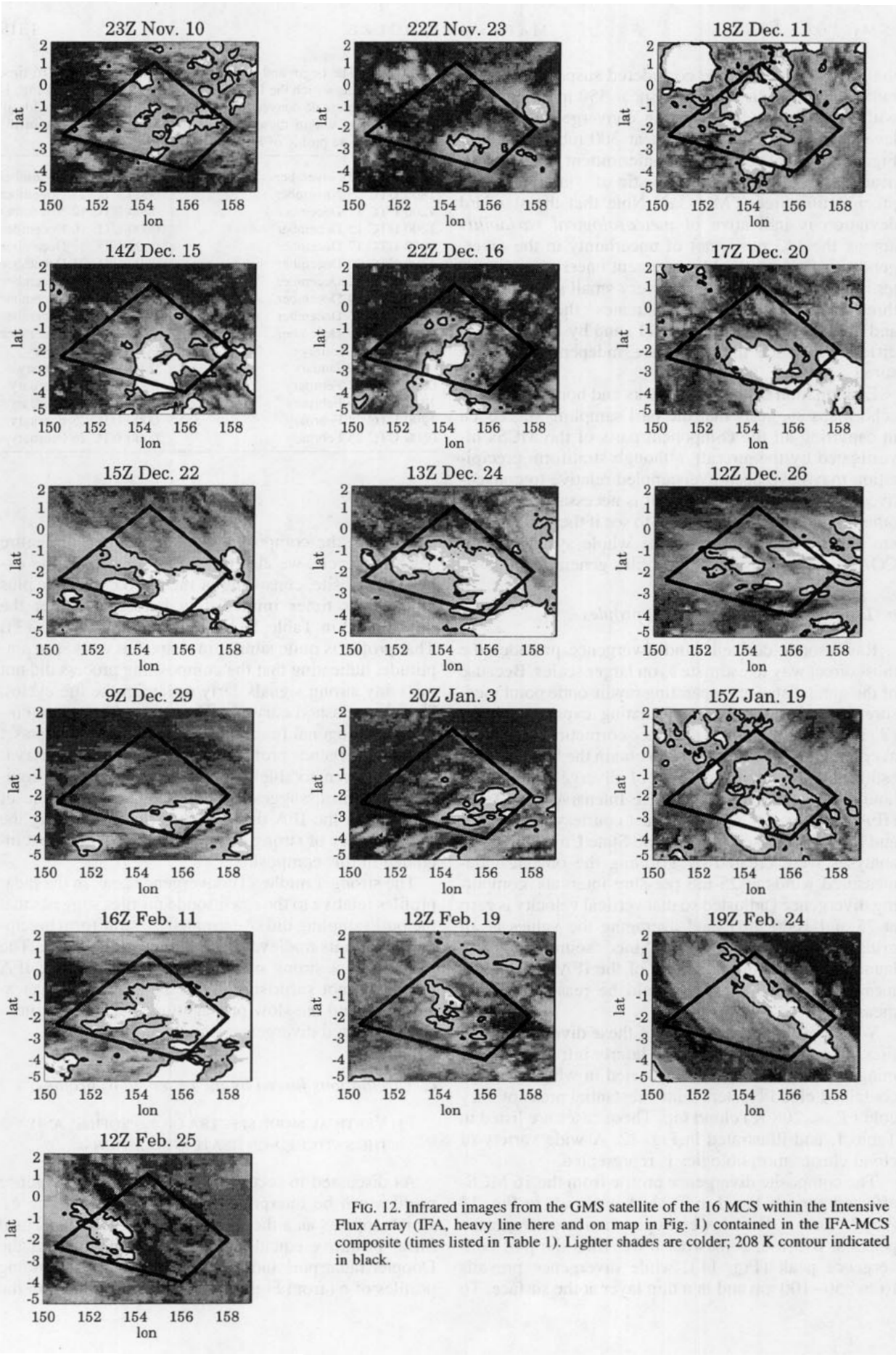

FIG. 12. Infrared images from the GMS satellite of the 16 MCS within the Intensive Flux Array (IFA, heavy line here and on map in Fig. 1) contained in the IFA-MCS composite (times listed in Table 1). Lighter shades are colder; 208 K contour indicated in black.

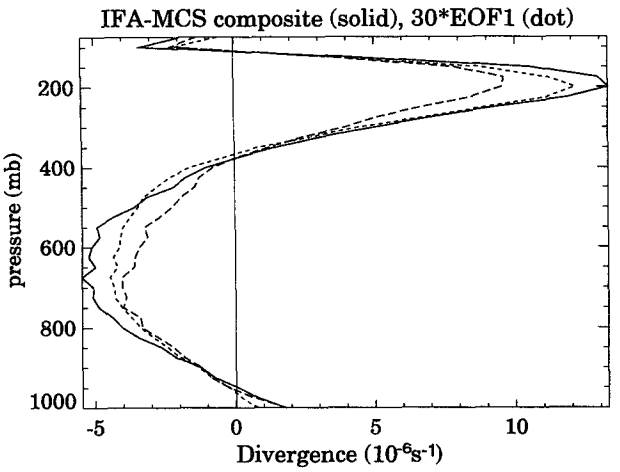

FIG. 13. Average IFA divergence profiles. Solid line: the IFA-MCS composite (Table 1, Fig. 12). Dashed line: the extended life cycle composite (IFA-MCS composite plus times immediately prior and subsequent to the times listed in Table 1). Dotted line: the leading EOF of the 480 IFA divergence profiles, arbitrarily scaled to match the other profiles.

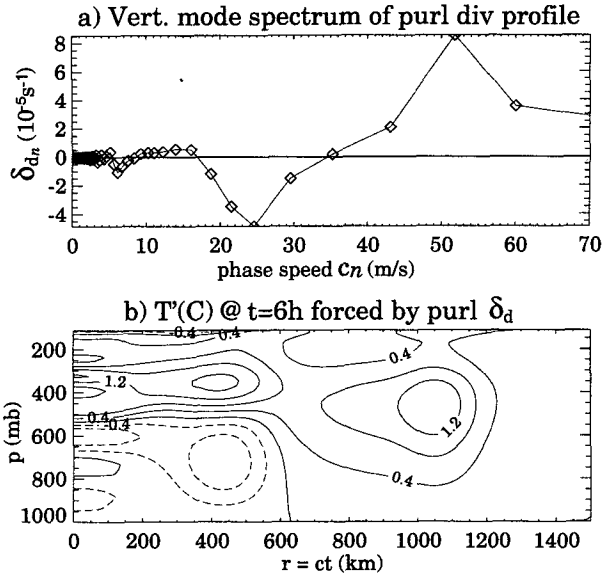

FIG. 14. (a) Vertical mode spectrum of the mean purl δ_d profile of Fig. 16. (b) Model temperature perturbation field six hours after the initiation of an imposed heat source characterized by the purl-derived δ_d profile. Contour interval 0.4°C, negative contours dotted. The heating magnitude corresponds to the δ_d values of Fig. 11a prevailing within a mesoscale area 140 km in radius (65 000 km^2, at the third-fourth quartile boundary in the MH93b cloud cluster size distribution). The radial distribution of δ_d is a cos^2 bell, which reaches zero at r = 140 km.

upper panels of Figs. 14a and 15a, respectively.[5] In the corresponding lower panels (Figs. 14b and 15b) are the temperature fields that would exist six hours after the impulsive startup of mesoscale (~150-km radius) heat sources with the corresponding δ_d profiles in a motionless, hydrostatic, nonrotating atmosphere. The correspondence between the features on the upper spectrum plots and the features in the temperature field is readily apparent, with the temperature field indicating also the vertical structures associated with each of the vertical modes.

All of the features in the temperature fields of Figs. 14b and 15b would be propagating left to right as internal gravity waves at the speeds indicated in the upper panels. Most notably, the deep subsidence warming near 1000-km radius propagates at ~50 m s^{-1}, and the warm above cool structure near 500 km propagates at ~24 m s^{-1}. The latter feature, with its adiabatic upward displacement of the whole lower troposphere up to 5 km, may favor the development of additional convection in the near-field environment of existing MCSs, making them naturally gregarious (Mapes 1993). Aircraft data from TOGA-COARE indicate that deep mesoscale temperature perturbations of >1°C do exist in the vicinity of MCSs (not shown). If the heating profile evolved in time, with the stratiform precipitation and its midlevel convergence lagging the deep convective portion of the heating, the temperature features in Figs. 14b and 15b would be horizontally smeared or at

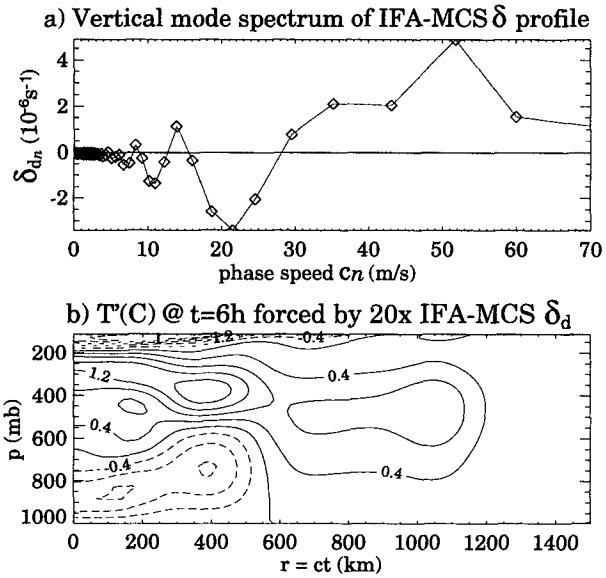

FIG. 15. As in Fig. 14, but for the IFA-MCS composite δ_d profile, with its amplitude increased by a factor of 20.

[5] Because the purl profile is not mass balanced, we retained only the convergent part of the profile (Fig. 11a with the unreliable 0–500-m layer value set to -0.5×10^{-4} s^{-1}) and spliced onto it a positive upper-tropospheric divergence consisting solely of the contributions from the 53 and 24 m s^{-1} modes. This procedure guarantees that poorly sampled upper-tropospheric δ features will not contribute to the vertical-mode spectrum.

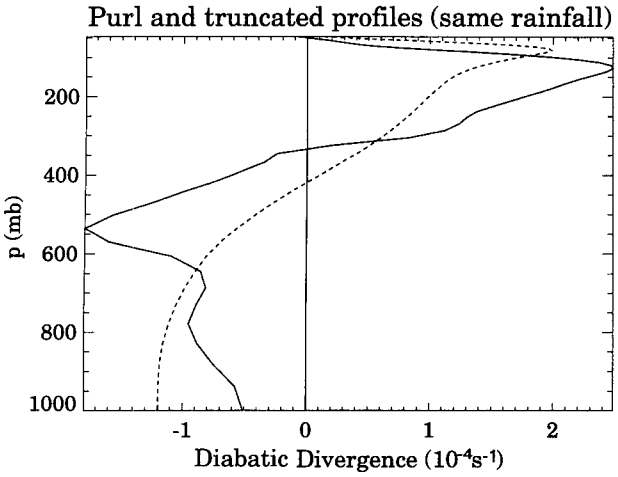

FIG. 16. Diabatic divergence profiles for the Hadley and Walker calculations. Solid: The purl δ_d profile from Fig. 11a, doctored at the surface and in the upper troposphere. Dashed: a spectral truncation retaining only the modes with $c > 40$ m s^{-1}. Both profiles represent the same amount of vertically integrated heating (rainfall).

slightly different radii, but the basic features would remain the same.

The temperature fields of Figs. 14b and 15b differ most strongly at radii < 200 km in the parts of the solution involving the high vertical wavenumbers in the δ_d profile. In particular, the melting-associated signal in the purl profile appears as a distinct peak in the spectrum at $c = 6$ m s^{-1} (Fig. 14a), which creates a wavelike temperature perturbation profile at 100-km radius within and near the heated region. The melting layer is anomalously cool, as expected, but the temperature reverberations in the vertical are unexpected. This result will be discussed further in section 6.

2) HADLEY AND WALKER CIRCULATIONS

The heating profile in tropical convection affects the vertical structures of thermally forced circulations from synoptic to planetary scales (e.g., Geisler and Stevens 1982; Hartmann et al. 1984; DeMaria 1985). The surface wind, important to ocean–atmosphere interactions, is of particular concern. This section illustrates, in an idealized way, some of the planetary-scale effects of the δ_d profile features measured in this study. In particular, we compare the circulations forced by the purl δ_d profile (Fig. 16, solid) and by a spectral truncation without the elevated convergence peak (dashed). The spectral truncation excludes all modes with $c < 40$ m s^{-1} and is equivalent to a Gill-type (1980) one-tropospheric-mode model with the same vertically integrated heating (i.e., the same rainfall rate).

Perhaps the simplest Walker circulation model is the analytic Gill (1980) solution, modified for multiple vertical modes by Geisler and Stevens (1982) [we note an error in the evaluation of the integral in their (21)]. Time-independent heating is imposed within a region 2500 km in the east–west direction and 2300 km (Gaussian e-folding width) in the north–south direction, and a steady state is sought with a linear damping coefficient of (5 days)$^{-1}$. Figure 17a shows the zonal wind field in the longitude–height plane for this steady-state version of the Walker circulation forced by the purl δ_d profile of Fig. 16, but with its amplitude divided by 15, to make magnitudes reasonable for this 2500-km-wide heated region. The elevated convergence maximum is fed by an elevated easterly inflow current, which deepens gradually with distance from the heated region until eventually the level of maximum wind is at the surface, 150° east of the heated region.

The surface wind is plotted in Fig. 17b for Walker circulations forced by the purl and truncated δ_d profiles. The fact that the convergence peaks aloft makes the Walker surface wind forced by the observed heating profile (solid line) considerably weaker than that forced by the truncated heating profile (dashed).

A similar dependence of surface wind upon the δ_d profile is evident in the zonal wind field in a friction-

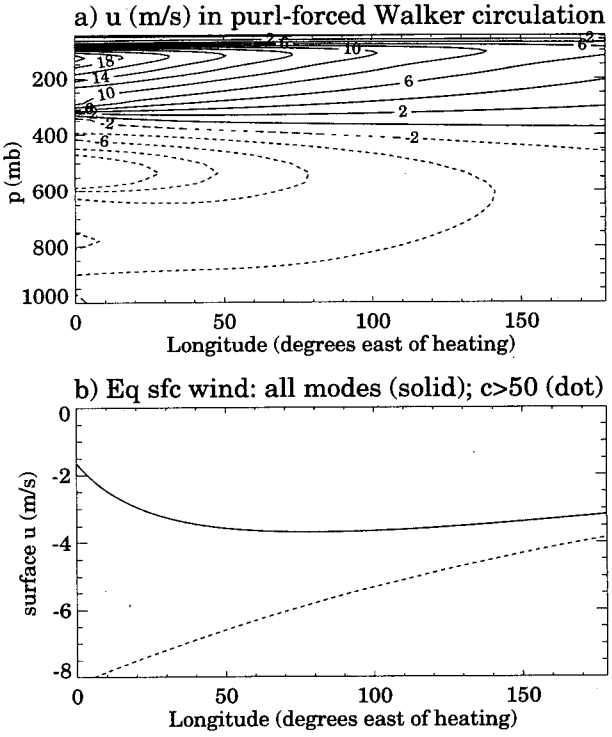

FIG. 17. Zonal wind in a Walker circulation. (a) Contoured zonal wind in the equatorial longitude–height plane for the multimodal version (Geisler and Stevens 1982) of the Gill (1980) solution for forced-damped steady-state circulation east of a region of imposed heating. The heating is 2500 km wide, located immediately to the west of this plot, with the purl δ_d profile of Fig. 16 divided by 15 to simulate the small fractional area coverage of MCSs on this 2500 km scale. (b) Surface winds over the same domain for the two δ_d profiles of Fig. 16 divided by 15.

less, zonally symmetric Hadley circulation on a β plane (Fig. 18a). In this case the heating was 2000 km wide, centered at 10° south, with the purl δ_d profile one-fiftieth of the amplitude shown in Fig. 16. Again, shallow features in the wind profile decay rather rapidly with distance from the heated region, so that the maximum wind is at the surface in regions far from the heating. Again, the full solution has substantially weaker surface winds than a solution for the truncated δ_d profile representing the same rainfall rate (Fig. 18b).

It is clear from these examples that the winds induced by atmospheric heating have a profile that locally matches the δ_d profile. This fact lends conceptual appeal to the use of δ_d rather than heating to characterize thermal forcing profiles. The surface wind weakness discussed above is indicative of the fact that surface convergence into west Pacific MCSs is weaker than the convergence aloft.

The strong convergence aloft and weak convergence or even divergence at the surface (Fig. 13) is indicative of the large downdraft mass fluxes in these west Pacific MCSs, both stratiform and convective (Fig. 3, Zipser 1977). In a sense, then, strong downdrafts in MCSs may account for weaker surface winds across large areas of the planet. Many TOGA-COARE analyses emphasize the fact that downdraft air reaching the marine boundary layer is anomalously cool, dry, and windy, and therefore causes sea–air thermal fluxes to increase in the local vicinity and wake of convection (e.g., Parsons et al. 1994). It is intriguing to speculate that these local downdraft-enhanced sea–air fluxes might be occurring at the expense of reduced sea–air fluxes elsewhere.

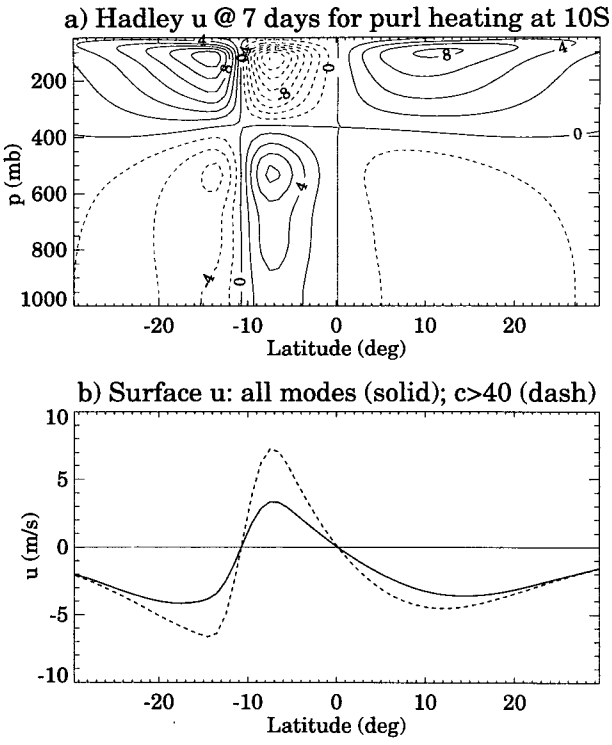

FIG. 18. Zonal wind in a zonally symmetric Hadley circulation. (a) Contoured zonal wind in the latitude–height plane after 7 days of heating in an adiabatic, frictionless atmosphere. The heating is 1000 km wide, centered at latitude −10, with the purl δ_d profile of Fig. 16 divided by 50. (b) Surface winds over the same domain for the two δ_d profiles of Fig. 16, divided by 50.

6. Response of convective δ_d to environmental temperature profiles

Three unusual aspects of the Doppler radar purl divergence observations—the case of 6 February, the "reverberations" above and below the melting level, and the spectral simplicity of the grand mean purl profile—deserve further comment, as they may all be consequences of a single mechanism: convective mass flux responding to the environmental temperature profile. In particular, convective heating adjusts its profile systematically to oppose temperature anomalies. Put another way, convection tends to preferentially detrain mass into anomalously stratified layers.

A number of nonexclusive explanations exist for this familiar property of convective clouds. These theories are of three distinct types, each based on different considerations of what clouds are or do. In descending order of the spatial scales on which explanations are sought, these are 1) profile maintenance theories (e.g., Manabe and Strickler 1964; Betts 1986; Bretherton and Smolarkiewicz 1989), based on the notion that convection acts to neutralize instability and restore some type of moist adiabatic stratification; 2) parcel theories, which invoke vertical stretching or compression of an air parcel by the variation of buoyancy through its depth (e.g., Taylor and Baker 1991); and 3) subparcel theories, which consider the buoyancy sorting of air created by turbulent and ultimately molecular mixing (e.g., Raymond and Blyth 1986, 1992; Cohen and Frank 1989; Kain and Fritsch 1990).

To our knowledge, *every existing convective parameterization scheme predicts temperature–anomaly-opposing heating profiles.* This fact is obvious for schemes that utilize in any way a specified reference profile (including moist convective adjustment schemes, the Betts–Miller scheme, and the Kuo scheme). Cohen and Frank (1989) showed that ensembles of plumes (which are the basis of a class of parameterization schemes) also act to damp environmental temperature anomalies. Likewise, the Emanuel scheme presumably damps temperature departures, like the Raymond and Blyth (1992) model upon which it is based. For details on convective parameterizations, consult Emanuel and Raymond (1994).

The mesoscale data examined in this paper are probably not sufficiently precise and quantitative to exclude any of these models or theories about the convective-scale mechanisms by which heating profiles come to

oppose environmental temperature anomalies. The purpose of this section is simply to illustrate three phenomena that arise from this important relationship.

a. The 6 February cyclone Oliver rainband

The unusual δ profiles from 6 February and the associated temperature anomalies were presented in section 4c(3), Figs. 8–10. This case is our most direct measurement of linked δ_d and temperature profile anomalies. But what was responsible for the observed temperature anomaly? One possible explanation is that developing cyclone Oliver, like the two 1987 Australian monsoon cyclones studied by Davidson et al. (1990), may have initially developed its maximum cyclonic circulation aloft near 3-km altitude. Oliver would then have had, from balanced flow considerations, a cool core below 3 km and warm core above. The initial circulation development aloft is consistent with the elevated peak in the low-level convergence into noncyclone MCSs in the warm-pool region (Fig. 13; Davidson et al. 1990; Fig. 9 of MH93a).

Davidson et al. showed that as the 1987 cyclones intensified, their circulation descended to the surface (also Fig. 20 of MH93a). The 6 February δ_d profiles indicate a possible mechanism for this downward development of elevated cyclones. The near-surface convergence anomaly, below the cool layer, acted to increase vorticity at that level, while the anomalous divergence near 3 km acted to decrease vorticity there. At the same time, the enhanced upward mass flux in the convection within the cool layer implies, by mass continuity, that enhanced subsidence warming was occurring elsewhere in the layer, outside the convection, tending to destroy the cool anomaly. In other words, *δ_d anomalies like those observed on 6 February act simultaneously on vorticity and thermal fields, in a way that would cause an initially elevated balanced circulation to develop downward.* This mechanism is summarized in schematic form in Fig. 19.

Of course, the actual 6 February cool temperature anomalies may not have been indicative of a cool core associated with cyclone Oliver some 400 km away. It may be that the 6 February anomalies were simply a particularly strong example of the melting reverberation phenomenon discussed below. But if the temperature sensitivity of the δ_d profile, evident in the 6 February data, is indicative of a systematic process in deep convective clouds, the downward development of cool-core cyclones is one inevitable consequence of that process.

b. Melting and its vertical reverberations

The melting reverberations seen in Doppler radar data [section 4c(2)] are one of the completely unexpected aspects of this study. The explanation for this phenomenon may also involve the mutual adjustment of convective δ_d and environmental temperature profiles.

Consider first the linear model T' field resulting from a prescribed meltinglike cooling alone (Fig. 20). The temperature perturbation after six hours of an imposed cooling at the melting level (same cylindrical geometry and contour interval as in Figs. 14–15) consists not only of cool temperatures at the melting level but of warm temperatures above and below it (Fig. 20c). This "sandwich" temperature profile is a result of the dispersive propagation of gravity waves in the atmosphere: a thin cooling causes a somewhat thicker layer of the atmosphere to descend, resulting in adiabatic warming above and below the cooled layer.[6]

An interesting sidelight here is the temperature perturbation profile 300 km from the center of the melting (Fig. 20d, dashed). It includes a rather deep warming throughout the layer beneath the melting level, reminiscent of the adiabatic downward displacements often seen at low levels near, but typically outside, stratiform rain regions ("onion soundings," Zipser 1977).

Convection penetrating a $+/-/+$ T' perturbation like that in Fig. 20c may be expected to develop δ_d features in quadrature with T', yielding a $+/-/+/-$ profile, as in the schematic Fig. 21. This melting-induced convective δ_d anomaly, in turn, could extend the wavelike T' profile, and so on. In this way, an imposed cooling at the melting level might, acting in concert with the heating profile of embedded convection, create an oscillatory pattern of δ_d and temperature anomalies in the vertical. This hypothesized mechanism for the development of melting reverberations in the MCS δ_d profile should be easily testable in convection-resolving models.

c. The spectral simplicity of the mean profile

The predominance of just two deep modes, in measurements with quite good vertical resolution, is rather striking (Fig. 14). Why are high wavenumbers, other than the melting-forced $c = 6$ m s^{-1} mode, so absent in the grand mean δ_d profile, when the individual profiles contributing to the mean have all kinds of high-amplitude vertical structures? Again, adjustment of δ_d profiles to temperature anomalies may explain this observation.

If a convective heating event occurs, with an arbitrary δ_d profile, the high vertical wavenumber features create shallow, slowly propagating temperature perturbations (as in Figs. 14b, 15b). Because they propagate so slowly, even small-amplitude high wavenumber

[6] The melting amplitude considered here is strong enough to create an unstable lapse rate (Fig. 20d, solid line). In nature, the resulting turbulent heat flux divergence would make the effective cooling felt by the hydrostatic mesoscale flow deeper than the layer in which melting strictly occurs.

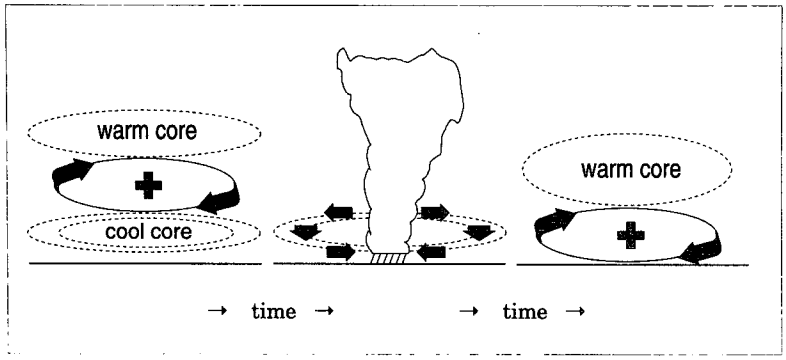

FIG. 19. Schematic diagram illustrating the possible role of anomalous MCS mass fluxes in the downward development of a cyclonic circulation. The circulation is initially centered near 3-km altitude, with a cool core below that level (left panel). Anomalous convergence and divergence in convection (horizontal arrows, middle panel), as observed on 6 February (Figs. 4, 5, 9), tend to lower the altitude of the vorticity maximum. Simultaneously the associated adiabatic subsidence (vertical arrows, middle panel) tends to destroy the cool temperature anomaly. As a result, the level of maximum circulation descends toward the surface, and a warm core develops at all levels (right panel).

contributions to the δ_d profile cause large-amplitude temperature anomalies to build up in the region near the convection (cf. Bretherton 1988). In an ongoing, organized MCS, the subsequent convection responds to the temperature anomalies created by the previous convection and tends to destroy them. By this self-adjustment or tuning process, in which shallow anomalies in one convective cell's δ_d profile cause opposite δ_d profile anomalies in subsequent or adjacent convective cells, the mean δ_d profile of mature MCSs may become very spectrally simple, as is observed.

Our arrival at this view of MCS δ_d profiles as self-adjusting was unanticipated at the outset of this study. But the constraint that MCS circulations must satisfy mass continuity with the stratified atmosphere in which they are embedded is a powerful one. It is not incorrect to attribute the bumps and wiggles on observed δ_d profiles to updrafts and downdrafts (as in Fig. 3) and hence to traditional cloud dynamical effects such entrainment, evaporation, water loading, etc. However, the results presented here seem to indicate that *the overall mean mass flux profile in mature MCSs is largely controlled*

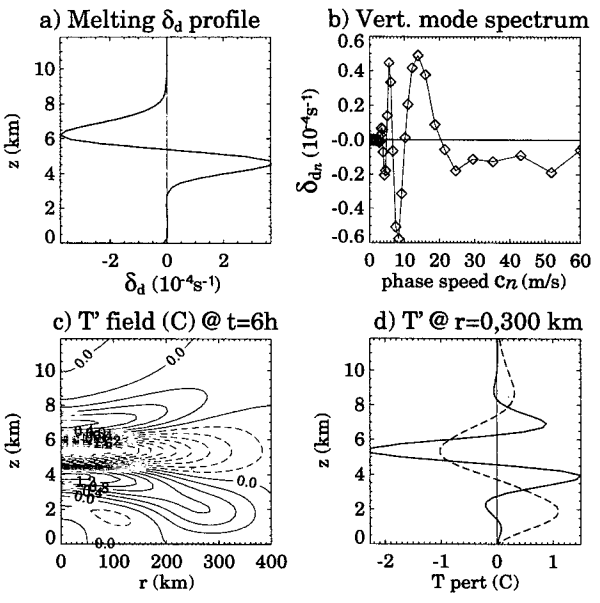

FIG. 20. The response of the linearized primitive equations to a mesoscale region of imposed melting-like cooling centered at 550 mb with 75-mb Gaussian half-width. (a) The δ_d profile of the imposed cooling. (b) The vertical mode spectrum of δ_d. (c) The temperature perturbation T' after six hours of cooling, computed as in Fig. 14 but with the δ_d profile from (a). Contour interval 0.2°C. (d) The T' profiles at $r = 0$ (solid) and 300 km (dashed).

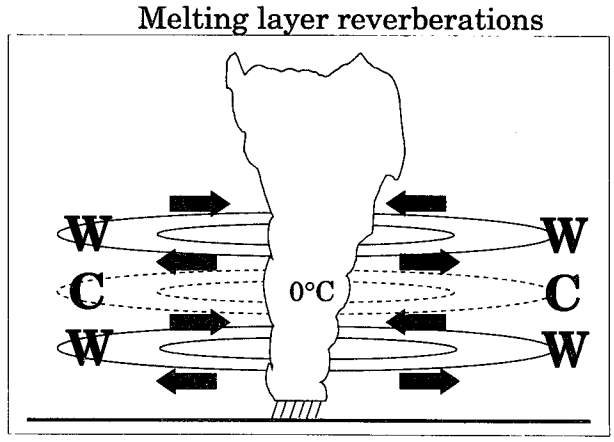

FIG. 21. Schematic view of the hypothesized development of melting reverberations. The melting creates a warm–cold–warm temperature anomaly, as in Fig. 20, to which convection responds with a div–conv–div–conv δ_d profile anomaly.

by the ability of the stratified environment to accept and distribute over the far-field fluid the mass redistribution implied by the δ_d profile. The complex internal thermodynamic processes in MCSs, primarily condensation and evaporation, conspire to adjust the total mean δ_d profile to forms readily accepted by the large-scale environment.

7. Summary and discussion

Diabatic divergence δ_d is the horizontal wind divergence that prevents temperature from changing in the presence of a diabatic heating. Inside tropical convective systems, the diabatic divergence greatly exceeds any adiabatic divergence, so divergence measurements can be interpreted as δ_d. Furthermore, thermal forcing in the primitive equations can be naturally expressed in terms of δ_d, so that divergence measurements can be directly used in diagnostic models of thermally forced circulations. Such an approach avoids the loss of information that typically occurs between heating profile measurement studies on the one hand and assessments of the large-scale impacts of heating profiles on the other.

Examination of airborne Doppler radar "purl" measurements in ten different MCSs observed during TOGA-COARE reveals a number of general features of MCS divergence profiles (Fig. 3), consistent with MH93a and earlier studies.

- Intense surface convergence into growing convective updrafts (frequently observed in low-level aircraft traverses of gust fronts) is largely counteracted, on average, by divergence in adjacent and subsequent downdrafts.
- As once-convective precipitation areas continue to age, they become more stratiform in character. The horizontal distribution of radar reflectivity becomes more uniform and a radar "brightband" develops near the melting level. The δ_d profile of stratiform areas is characterized by midlevel convergence, with an intense, shallow "melting convergence" peak at the 0°C level.
- Doppler radar, as a rule, fails to measure completely the divergence in the upper troposphere, even in cases of very deep echo. Much of the air diverging aloft is echo-free air moving aside to make way for ascending air, in both convective and stratiform situations.

Larger-scale MCS composite divergence profiles from the COARE Intensive Flux Array (IFA, Fig. 1) generally agree with the mean of the Doppler purl measurements, although stratiform precipitation may have been somewhat oversampled by the aircraft (cf. Figs. 11, 13). While not necessarily representative of all COARE-region convective heating, MCS heating is of particular importance as a *perturbation* heating for studies of diurnal and intraseasonal oscillations. Satellite studies indicate that large cloud clusters are modulated more than small ones by intraseasonal variation and that they contribute almost all of the diurnal cycle of cold cloudiness (Mapes and Houze 1993b).

The Doppler radar–observed mean δ profile consists to a remarkable degree of just the two deepest internal modes spanning the troposphere (Fig. 14a). It is postulated that this spectral simplicity is not coincidental but rather reflects a tight coupling on the mesoscale between δ_d-induced temperature perturbations on the one hand and T'-induced δ_d perturbations on the other. Because in an MCS each convective element rises through, and acts to damp, the temperature perturbations created by previous convective elements, the high wavenumber features seen in instantaneous δ profiles do not persist in the average. In this way, mean MCS δ_d profiles, highly constrained by the ability of the larger-scale atmosphere to accept mass redistribution, grow to lack almost totally any high vertical wavenumber features.

The exception that proves the rule comes from the melting of snow, which invariably takes place within a shallow, fixed layer in the atmosphere. A linear primitive equation model indicates that this type of mesoscale cooling generates a cool layer sandwiched between warm layers: the beginnings of a reverberation pattern in the vertical. Subsequent convection responds to the temperature profiles, as in Fig. 21, and the reverberation pattern in δ_d (Fig. 14b), continuously forced by melting, grows to extend throughout the troposphere. An additional feature of the melting-induced T' field is adiabatic downward displacement in the lower troposphere in regions near, but not under, the melting (Fig. 20). This seems to be the linear version of the "onion sounding" (Zipser 1977) frequently observed in the environment of stratiform rain regions.

Unusual temperature and δ_d profiles in the cyclone rainband of 6 February illustrate how the δ_d profile interacts with environmental temperature perturbations. Anomalous upward mass flux and heating in the rainband acted in the sense of destroying the low-level "cool core" temperature anomaly observed by aircraft and dropsondes. At the same time, the associated horizontal divergence acted to enhance the surface vorticity at the expense of vorticity near the 3-km level. This process, schematically shown in Fig. 19, could explain the downward development of tropical cyclones, as is frequently observed in the region (Davidson et al. 1990).

Finally, linear models of thermally forced Hadley and Walker circulations show the dependence of large-scale surface winds (without a boundary layer) on the δ_d profile of a specified heat source. A Gill-type truncation of the δ_d profile greatly overpredicts surface winds, compared to the measured MCS δ_d profile representing the same amount of heating (rainfall). The elevated convergence into MCSs is therefore of great importance to planetary-scale circulations and climate (as shown earlier by Hartmann et al. 1984). Since this

elevated convergence largely feeds into convective and mesoscale downdrafts, the question arises whether the remote, planetary-scale climate effects of downdrafts in MCSs might exceed their well-known importance to the local boundary-layer climate.

It remains unclear what processes control the relative amplitudes of the two main modes of the mean MCS δ_d profile. This question is probably related to the relative amounts of convective versus stratiform rainfall (Houze 1989). The answer bears strongly on the determination of bulk precipitation efficiency or updraft to downdraft mass-flux ratio parameters required by some theories of tropical convection (Emanuel et al. 1994; Raymond 1995). The tropical Atlantic and Pacific regions differ significantly in this regard (e.g., Frank and McBride 1989). Do these regional differences arise from the different geography and sea surface temperature patterns somehow? Or perhaps they come from different radiative destabilization profiles? Whatever mechanisms are involved, the strange phenomenon of melting reverberation cautions that the answers to these questions may be nonlocal in the vertical.

Acknowledgments. Drs. Frank Marks and David Jorgensen, along with flight directors Jack Parrish and Phil Bogart, guided the aircraft purl sampling to its success. The NOAA WP-3D pilots and aircrews spent many hours flying skillfully and cheerfully in circles for this study. Xin Lin and Dick Johnson generously provided their analyses of the IFA rawinsonde data. Mark DeMaria provided the Fulton and Schubert (1985) vertical transform software. Dave Raymond and two anonymous reviewers helped improve the manuscript. This research was supported by NSF Grant ATM9024431, by the NOAA Global Change Fellowship Program via the UCAR Office of Programs, and by the TOGA COARE International Project Office.

REFERENCES

Betts, A. K., 1986: A new convective adjustment scheme. Part I: Observational and theoretical basis. *Quart. J. Roy. Meteor. Soc.*, **112,** 677–691.

Bretherton, C. S., 1988: Group velocity and the linear response of stratified fluids to internal heat or mass sources. *J. Atmos. Sci.*, **45,** 81–93.

——, and P. K. Smolarkiewicz, 1989: Gravity waves, compensating subsidence, and detrainment and detrainment around cumulus clouds. *J. Atmos. Sci.*, **46,** 740–759.

Cifelli, R., and S. A. Rutlege, 1994: Vertical motion structure in maritime continent mesoscale convective systems: Results from a 50-MHz profiler. *J. Atmos. Sci.*, **51,** 2631–2652.

Cohen, C., and W. M. Frank, 1989: A numerical study of lapse-rate adjustments in the tropical troposphere. *Mon. Wea. Rev.*, **117,** 1891–1905.

Davidson, N. E., G. J. Holland, J. L. McBride, and T. D. Keenan, 1990: On the formation of AMEX cyclones Irma and Jason. *Mon. Wea. Rev.*, **118,** 1981–2000.

DeMaria, M., 1985: Linear response of a stratified tropical atmosphere to convective forcing. *J. Atmos. Sci.*, **42,** 1944–1959.

Emanuel, K. A., and D. J. Raymond, Eds., 1994: *The Representation of Cumulus Convection in Numerical Models of the Atmosphere. Meteor. Monogr.*, No. 46, Amer. Meteor. Soc., 246 pp.

——, J. D. Neelin, and C. S. Bretherton, 1994: On large-scale circulations in convecting atmospheres. *Quart. J. Roy. Meteor. Soc.*, **120,** 1111–1143.

Frank, W. M., and J. L. McBride, 1989: The vertical distribution of heating in AMEX and GATE cloud clusters. *J. Atmos. Sci.*, **46,** 3464–3478.

Fulton, S. R., and W. H. Schubert, 1985: Vertical normal mode transforms: Theory and application. *Mon. Wea. Rev.*, **113,** 647–658.

Geisler, J. E., and D. E. Stevens, 1982: On the vertical structure of damped steady circulation in the tropics. *Quart. J. Roy. Meteor. Soc.*, **108,** 87–93.

Gill, A. E., 1980: Some simple solutions for heat-induced tropical circulation. *Quart. J. Roy. Meteor. Soc.*, **106,** 447–462.

Hartmann, D. L., H. H. Hendon, and R. A. Houze Jr., 1984: Some implications of the mesoscale circulations in tropical cloud clusters for large-scale dynamics and climate. *J. Atmos. Sci.*, **41,** 113–121.

Houze, R. A., Jr., 1982: Cloud clusters and large-scale vertical motions in the tropics. *J. Meteor. Soc. Japan,* **60,** 396–410.

——, 1989: Observed structure of mesoscale convective systems and implications for large-scale heating. *Quart. J. Roy. Meteor. Soc.*, **115,** 425–461.

——, 1993: *Cloud Dynamics.* Academic Press, 570 pp.

——, B. F. Smull, and P. Dodge, 1990: Mesoscale organization of springtime rainstorms in Oklahoma. *Mon. Wea. Rev.*, **118,** 613–654.

Janowiak, J. E., P. A. Arkin, and M. Morrissey, 1994: An examination of the diurnal cycle in oceanic tropical rainfall using satellite and in situ data. *Mon. Wea. Rev.*, **122,** 2296–2311.

Kain, J. S., and J. M. Fritsch, 1990: A one-dimensional entraining/detraining plume model and its application in convective parameterization. *J. Atmos. Sci.*, **47,** 2784–2802.

Kasahara, A., 1984: The linear response of a stratified global atmosphere to tropical thermal forcing. *J. Atmos. Sci.*, **41,** 2217–2237.

Leary, C. A., and R. A. Houze Jr., 1979: The structure and evolution of convection in a tropical cloud cluster. *J. Atmos. Sci.*, **36,** 437–457.

Manabe, S., and R. F. Strickler, 1964: Thermal equilibrium of the atmosphere with a convective adjustment. *J. Atmos. Sci.*, **21,** 361–385.

Mapes, B. E., 1993: Gregarious tropical convection. *J. Atmos. Sci.*, **50,** 2027–2037.

——, and R. A. Houze Jr., 1992: Satellite-observed cloud clusters in the TOGA-COARE domain. *TOGA Notes,* **7,** 5–7.

——, and ——, 1993a: An integrated view of the 1987 Australian monsoon and its mesoscale convective systems. Part II: Vertical structure. *Quart. J. Roy. Meteor. Soc.*, **119,** 733–754.

——, and ——, 1993b: Cloud clusters and superclusters over the oceanic warm pool. *Mon. Wea. Rev.*, **121,** 1398–1415.

Ooyama, K. V., 1971: A theory on the parameterization of cumulus convection. *J. Meteor. Soc. Japan,* **49,** 744–756.

Parsons, D., and Coauthors, 1994: The Integrated Sounding System: description and preliminary observations from TOGA COARE. *Bull. Amer. Meteor. Soc.*, **75,** 553–567.

Raymond, D. J., 1983: Wave-CISK in mass flux form. *J. Atmos. Sci.*, **40,** 2561–2572.

——, 1995: Regulation of moist convection over the warm tropical ocean. *J. Atmos. Sci.*, submitted.

——, and A. M. Blyth, 1986: A stochastic mixing model for nonprecipitating cumulus clouds. *J. Atmos. Sci.*, **43,** 2708–2718.

——, and ——, 1992: Extension of the stochastic mixing model to cumulonimbus clouds. *J. Atmos. Sci.*, **49,** 1968–1983.

——, R. Solomon, and A. M. Blyth, 1991: Mass fluxes in New Mexico mountain thunderstorms from radar and aircraft measurements. *Quart. J. Roy. Meteor. Soc.*, **117,** 587–621.

Ruprecht, E., and W. M. Gray, 1976: Analysis of satellite-observed cloud clusters. Part I: Wind and dynamics fields. *Tellus,* **28,** 391–413.

Schubert, W. H., P. E. Ciesielski, D. E. Stevens, and H. Kuo, 1991: Potential vorticity modeling of the ITCZ and the Hadley circulation. *J. Atmos. Sci.,* **48,** 1493–1509.

Sui, C. H., K. M. Lau, W. K. Tao, and J. Simpson, 1994: The tropical water and energy cycles in a cumulus ensemble model. Part I: Equilibrium climate. *J. Atmos. Sci.,* **51,** 711–728.

Taylor, G. R., and M. B. Baker, 1991: Entrainment and detrainment in cumulus clouds. *J. Atmos. Sci.,* **48,** 112–121.

TCIPO, 1992: *TOGA-COARE Operations Plan.* TOGA-COARE International Project Office, Boulder, CO.

Webster, P. J., and R. Lukas, 1992: TOGA COARE: The Coupled Ocean–Atmosphere Response Experiment. *Bull. Amer. Meteor. Soc.,* **73,** 1377–1416.

Williams, C., 1994: Analysis of deep convective clouds and their association with non-migrating atmospheric diurnal tides in the tropical troposphere. NOAA Tech. Memo. ERL AL-13, 194 pp.

Yanai, M., S. Esbensen, and J.-H. Chu, 1973: Determination of bulk properties of tropical cloud clusters from large-scale heat and moisture budgets. *J. Atmos. Sci.,* **30,** 611–627.

Yuter, S. E., and R. A. Houze Jr., 1995: Three-dimensional kinematic and microphysical evolution of Florida cumulonimbus. Part II: Frequency distributions of vertical velocity, reflectivity, and differential reflectivity. *Mon. Wea. Rev.,* **123,** 1941–1963.

Zipser, E. J., 1977: Mesoscale and convective-scale downdrafts as distinct components of squall-line circulation. *Mon. Wea. Rev.,* **105,** 1568–1589.